energies

MDPI

Article

Boiling Heat Transfer during Flow in Vertical Mini-Channels with a Modified Heated Surface

Magdalena Piasecka * and Kinga Strąk

Faculty of Mechatronics and Mechanical Engineering, Kielce University of Technology, 25-314 Kielce, Poland
* Correspondence: tmpmj@tu.kielce.pl; Tel.: +48-41-342-4320

Abstract: The process with change of phase during flow in mini-channels plays a significant role in many industrial applications, such as microelectronics. Furthermore, methods for heat transfer intensification during flow in channels of small cross-section are still being sought. In this work, studies of the effect of using a modified heated surface on intensification boiling heat transfer in rectangular mini-channels during upward and downward flow are performed. The test section of a group of seven parallel mini-channels 1 mm deep was investigated during the subcooled and saturated flow boiling of FC-72. The temperature of the outer heated wall surface was measured using an infrared camera. During the experiments, two-phase flow structures were captured with a quick camera. Local heat transfer coefficients at the contact surface between the working fluid and the heated surface were determined with the use of a one-dimensional calculation method. To present the results, local temperature measurements and heat transfer coefficients, boiling curves and two-phase flow patterns are shown and analyzed. The results concerning two directions of vertical flow along mini-channels are discussed. Several modified heated surfaces and one smooth were tested for comparison. The main objective was to find out how the modified surface of the heated wall can intensify boiling heat transfer with upward and downward refrigerant flow in mini-channels of rectangular cross-section.

Keywords: mini-channel; flow boiling; modified heated surface; heat transfer intensification; two-phase flow structures

Citation: Piasecka, M.; Strąk, K. Boiling Heat Transfer during Flow in Vertical Mini-Channels with a Modified Heated Surface. *Energies* **2022**, *15*, 7050. https://doi.org/10.3390/en15197050

Academic Editor: Phillip Ligrani

Received: 31 August 2022
Accepted: 22 September 2022
Published: 26 September 2022

1. Introduction

The dimensions of the channel are of great importance in the process of flow boiling heat transfer. Depending on the size of the channel cross-section, different physical phenomena take place during flow. In the literature, there are many types of channel classifications. Shah presented one of the main classifications of channels [1], which includes two main groups: mini-channels (d_h less than 6 mm) and conventional channels (d_h greater than 6 mm).

Kandlikar [2] proposed a new classification of channels. According to this classification, the channels were divided into three groups, taking into account the hydraulic diameter, that is: conventional ($d_h > 3$ mm), mini- (200 µm $< d_h \leq 3$ mm) and micro- (10 µm $< d_h \leq 200$ µm) channels.

For more than a dozen years, the impact of experimental parameters (geometrical, thermal-flow, pressure) on boiling heat transfer has been widely discussed in the literature. Many aspects of this issue are still not clear, and the results related to modified walls are still studied.

The purpose of the study described in Ref. [3] was to research subcooled flow boiling heat transfer water in a mini-channel with dimensions of 45 mm × 2 mm × 2 mm and graphene nanostructured surfaces. The two superhydrophilic surfaces, named GNPs/SE (I) and GNPs/SE (II), at low mass flux, showed maximum heat flux enhancements of 24.5% and 59.5%, compared to the uncoated surface. Furthermore, the enhanced coatings helped achieve higher values of the heat transfer coefficient, 20.1% and 64.9%, compared to the

plain surface. The authors stated that using superhydrophilic GNP coatings has an impact on effective film boiling heat transfer and the fast water permeation effect. According to the authors, during development of boiling, the coatings caused bubble detachment and blocked dry spot formation. One of the tested GNPs coatings, i.e., the CE (I) surface, showed more nucleation sites and bubbles ready to detach compared to that of the uncoated surface. It was also underlined that, for the mini-channels with both tested coatings, with a decrease in liquid subcooling, an increasing heat flux removal rate was obtained.

The authors of Ref. [4] focused on flow boiling heat transfer in a rectangular channel vertically positioned, heated from one side and the other with modified surface by using a femtosecond laser texture. The laser was used to texture the surface to change its wettability. It was noticed that the hydrophobic surface delayed the nucleate boiling initiation, in comparison to that of the hydrophilic surface, whereas the boiling curves were shifted to higher wall superheat. It was recognized that the use of the hydrophobic surface in the research caused lower critical heat flux (20%). Moreover, less sensitivity to changes in subcooling was indicated for such a surface.

In Ref. [5], flow boiling heat transfer of carbon dioxide was investigated in macro- and micro-scale channels with pure CO_2 and CO_2/lubricant mixtures. The authors discussed the experimental results for smooth and enhanced tubes with the use of known correlations from the literature. Under the same operating conditions, the two-phase heat transfer coefficients in the micro-fin tubes were significantly higher (up to +500%) compared to smooth tubes. The authors noticed that the micro-fin structure generated the liquid phase, increasing turbulence. For the enhanced tubes, good agreement was obtained only with the Mehendale correlation (2018), proposed for numerous fluids.

The studies discussed in Ref. [6] refer to water flow boiling heat transfer in micro-channels using several surfaces: smooth, micro-fin and micro-cavity. In that study, the authors used the numerical method to examine flow boiling on tested micro-structured surfaces. Based on the results, it was noticed that compared to a smooth surface with an angle of 60°: (i) the micro-fin surface had lower thermal resistance (36.64%) and a higher heat transfer coefficient (61.92%); (ii) the micro-cavity surface had lower thermal resistance (13.55%) and a higher heat transfer coefficient (17.16%). Furthermore, it was noticed that the heat transfer performance was enhanced for the smooth and micro-cavity surfaces, when the dryout area and the wettability of the modified heating surface was minimized.

In Ref. [7], the flow boiling heat transfer of graphene nanoplatelets nanosuspension was examined. A small copper disk was used in the research as a test surface. It was noticed that the presence of graphene oxide nanoplatelets (GNPs) caused a decrease in the flow boiling heat transfer process over 1000 min of continuous operation (after the critical heat flux point). The authors' point of view was that it was mainly due to the heat accumulation on the surface caused by the existence of graphene oxide on the test surface. Furthermore, heat transfer increased with increasing heat flux and flow rate. It was stated that the increase in heat transfer occurred because of the intensification of the Brownian motion. Moreover, the thermophoresis effect in the boiling micro-layer close to the surface was indicated.

R134a flow boiling heat transfer studies on a nanocomposite coating (graphene–Cu) on a copper substrate were presented in Ref. [8]. The graphene–Cu nanocomposite powders were made using a mechanical alloying technique with the use of ball mills (0, 10, 20 and 30 vol%). In the test section, a rectangular channel 60 mm wide, 3 mm high and 460 mm long was produced. The dimensions of the graphene–Cu composite test plates were 10 mm × 10 mm. In studies with a higher graphene concentration, the heat transfer coefficient and higher heat flux were obtained. Additionally, during an increase in mass flux, an increase in flow boiling heat transfer was observed.

The authors of Ref. [9] referred to studies on deionized water flow boiling heat transfer in a high-aspect-ratio groove-wall micro-channel of dimensions: 200 μm height, 80 μm width and 10 mm length. Furthermore, the results were discussed with the plain side walls. The studies were carried out for two inlet subcoolings (40 °C and 70 °C), three values of

mass flux (446, 630 and 815 kg/(m^2·s)) and heat fluxes in the range of 3.8–139.5 W/cm^2. The groove-wall micro-channel in the two-phase flow region caused an earlier boiling initiation, a higher heat transfer coefficient and a lower pressure drop in comparison to the plain-wall one. Compared to the plain-wall micro-channel, when the results obtained for all set mass fluxes and inlet subcoolings were analyzed, the heat transfer coefficient for the groove-wall micro-channel enhancements was higher, from 25.0% to 56.7%.

Ref. [10] dealt with deionized water flow boiling in a groove-wall micro-channel. The main experimental parameters were as follows: mass flux in the range of 446–963 kg/(m^2·s) and heat flux in the range of 36.3–502.8 W/cm^2. The micro-channels had the following dimensions: height of 200 μm; groove spacing ratios of 2, 5 and 8; and groove depths of 15, 30 and 45 μm. The silicon-based channel aspect ratios were 1, 2.5 and 4. The results for enhanced micro-channels were compared with those gained for plain-wall micro-channels. The average heat transfer coefficient was found to change moderately with different spacing ratios or groove depths, and considerably with the channel aspect ratio. It was noticed that the heat transfer coefficient increased and then subsequently decreased for the groove spacing ratio or the groove depth increase. For the groove-wall channel, the best heat transfer enhancement was obtained at an aspect ratio of 2.5. The authors stated that the number of grooves and depths has a small impact on pressure drops.

Studies of flow boiling heat transfer deionized water on wettability-patterned surfaces. were presented in Ref. [11]. The test surfaces were characterized by hydrophobic-patterned arrays in the shape of a circle, triangle and inverted triangle on a SiO_2—hydrophilic substrate. The experimental parameters were: mass flow rate of 0.51 kg/min, a Reynolds number equaling 6000 and inter-spacing between neighboring nucleation sites of 0.75 mm or 1 mm. Compared to a homogeneous Si-surface, the surface with hydrophobic-patterned arrays indicated an improvement in flow boiling heat transfer for the critical heat flux (40–43%) and the heat transfer coefficient (35–163%). The triangle hydrophobic-patterned array surface caused a higher heat dispassion capacity of about 47% and 16% compared to the surfaces with hydrophobic patterns with circle and inverted- triangle shapes, respectively. At the high heat flux region, the hydrophobic patterns caused the flow boiling heat transfer processes.

In Ref. [12], research was conducted on subcooled flow boiling water with hybrid submillimeter/micro/nanostructured surfaces dedicated to plasma-facing components (PFCs) in nuclear fusion engineering. According to the authors, such surfaces help to achieve subcooled flow boiling enhancement and low flow resistance. It was stated that compared to the smooth surface at the same wall superheat, while multilayered hybrid surfaces were applied, the heat flux was 2~3-fold higher, and the critical heat fluxes increased by 80–200%. Furthermore, it was noticed that the maximum pressure drop increased by less than 12%. For the manipulated surfaces, the heat transfer coefficients were at least twice as high compared to the smooth surface.

At the Kielce University of Technology in Poland, for several dozen years, experimental and/or theoretical studies of flow boiling heat transfer in mini-channels were performed. In the experiments, the test sections with smooth and enhanced surfaces [13–18] were used while various cooling liquids were working fluids and the changeable spatial orientation of the test sections was applied, as described, e.g., in Refs. [13,19]. Furthermore, pool boiling heat transfer research using modified heated surfaces with fins, as with open micro-channels, was the subject of numerous publications. Examples of works presented with the results of this topic can be found in Refs. [20–23].

According to the short literature review presented, it is clear that results concerning boiling heat transfer during cooling fluid flow in mini-channels are inconsistent and even contradictory. The effects of direction of flow and channel spatial orientation have not yet been thoroughly recognized. The results cited in the literature usually cover only a few working fluids. There is often a lack of information on the interconnection between the two-phase flow patterns with temperature distributions across the heater surfaces and the fluid temperature distribution in mini-gaps. New investigations into the impacts of the use

of enhanced heated surfaces at fixed thermal and flow parameters in the entire range of nucleate boiling are still needed.

This work presents the results of a study on subcooled and saturated boiling heat transfer during Fluorinert FC-72 flow in seven parallel mini-channels of 1 mm depth, resistively heated by a common metal wall. The results of steady-state experiments with a modified heated wall surface produced in various processes: electro-machining texturing, laser surface texturing and iron powder soldering, and using emery papers of different roughness (P-36, P-80, P-220, P-389), are discussed. The purpose of this paper is mainly to recognize the influence of the modified heated surface of the channel wall and the orientation of the mini-channel (upward and downward flow) on intensifying heat transfer processes during flow in a mini-channel.

2. The Experimental Setup

The main systems of the experimental setup concerning research flow boiling heat transfer in the mini-channel test section are presented in Figure 1.

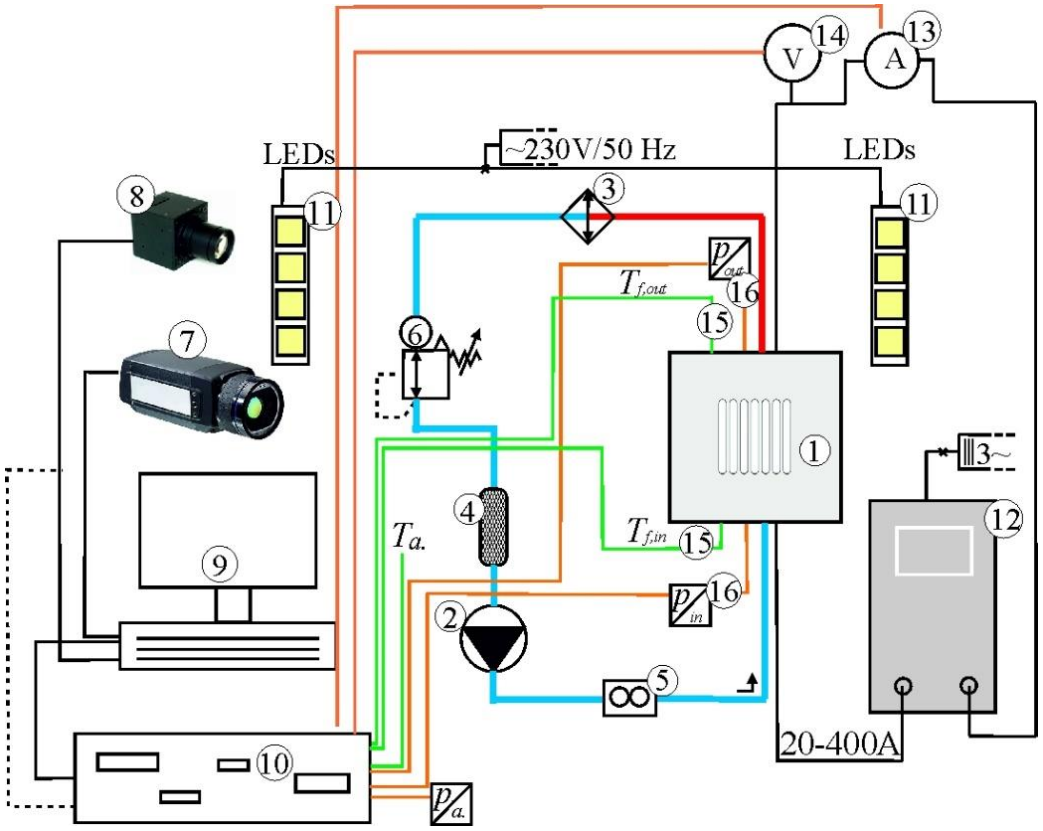

Figure 1. The experimental stand—a schematic diagram: 1—a test section with a group of mini-channels, 2—a gear pump, 3—a heat exchanger, 4—a filter, 5—a Coriolis mass flowmeter, 6—an air separator, 7—an infrared camera, 8—a high-speed video camera, 9—a PC computer, 10—data acquisition stations, 11—LED lighting system, 12—a power supply, 13—an ammeter, 14—a voltmeter, 15—a thermocouple, 16—a pressure meter.

The experimental setup was composed of the following systems (Figure 1): the main loop with working FC-72 fluid; the data and image acquisition system with the lighting system; and the power supply and control system. The essential component of the main loop is a test section with a group of rectangular mini-channels. The test section was vertically oriented, with upward and downward flows set (1). The other elements of the main loop were: a gear pump (2), a heat exchanger (3), a filter (4), a Proline Promass A 100 Coriolis mass flowmeter (5) and an air separator (6). The data and image acquisition system

included the following devices: an infrared camera A655SC FLIR with accuracy ±2 °C or ±2% at measuring temperature range (7), a high-speed video camera SP-50 0 0M-CXP2 (8), a PC computer (9) and two data acquisition stations (DaqLab 2005 and MCC SC-1608G) (10). A lighting system consisting of LEDs (11) was used to illuminate the flow of the working fluid along the mini-channels. The power supply and control system consisted of: a power supply (12), an ammeter (13) and a voltmeter (14). K-type thermocouples (15) and PMP71 Cerabar S pressure meters (16) were located at the inlet and outlet of the mini-channels.

The schematic diagrams of the test section are shown in Figure 2.

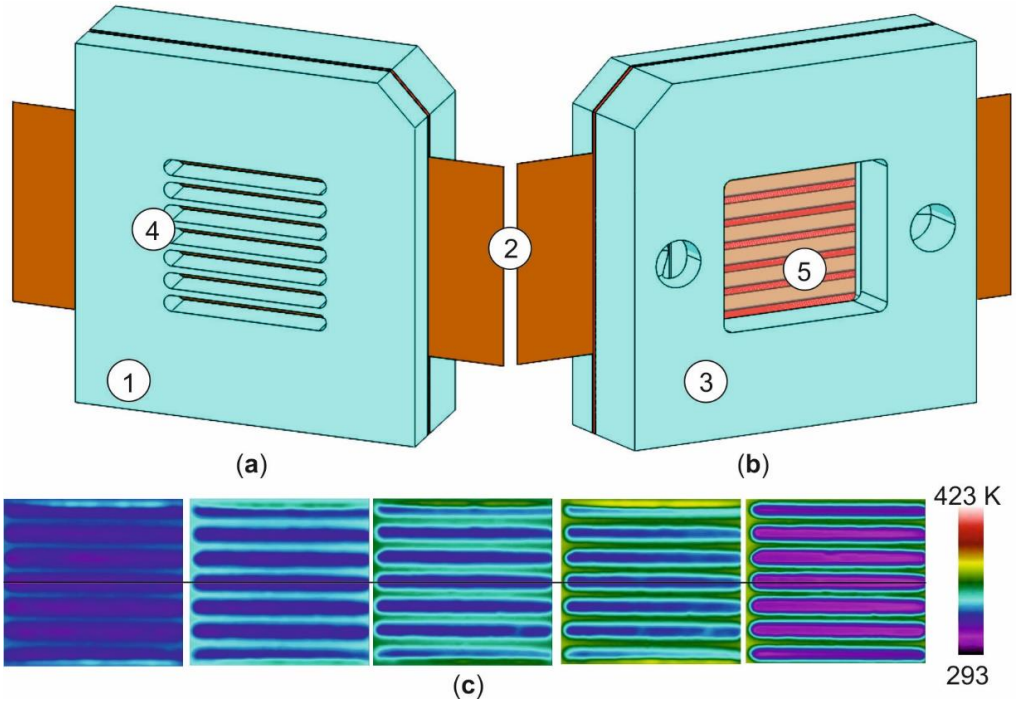

Figure 2. (**a**,**b**) Schematic diagrams of the test section: (**a**) view of the smooth side of the heated plate, (**b**) view of the modified side of the heated plate; 1—a top cover, 2—a heated plate, 3—a body, 4—system of channels in the cover to prevent deformation of the heated plate, 5—a glass plate; (**c**) example thermograms captured during experimental series when heat flux increased (the experiment with the smooth heated plate, mass flux of 566 kg/(m^2·s), downward flow 270°).

In the test section (Figure 2a,b), there were seven parallel mini-channels (4) comprising a common heated plate about 0.10 mm thick (2) with a modified surface contacting the working fluid. Other main components of the test section were: a top cover with the system of channels to prevent deformation of the heated plate (1), a body (3) and a glass plate (5). Each mini-channel was 1 mm deep and 6 mm wide, while their length, corresponding to the recorded temperature field, was 32 mm. The heated plate was made of Haynes-230 alloy. The thermograms on its outer side were recorded by an infrared camera. This smooth plate surface was coated with black paint of known emissivity (about 0.97). Example thermograms of experimental series are illustrated in Figure 2c. The flow pattern was observed through the glass plate from the modified heated plate surface being in contact with the fluid. During the experimental sets, the vertical test section was investigated, with upward flow of the fluid (position named 90°) or downward flow (position named 270°).

The ranges of experimental thermal and flow parameters are listed in Table 1.

Table 1. Experimental thermal and flow parameters.

Parameter	Range of Values/Values
Heat Flux, q_w (kW/m^2)	31.1–54.2
Mass Flux, G (kg/(m^2·s))	284 and 566
Inlet Pressure, p_{in} (kPa)	115–142
Inlet Liquid Subcooling, ΔT_{sub} (K)	41–46

3. Characteristics of the Modified Heated Plate Surface

The main aim of this work is to investigate the influence of the use of modified heated surfaces on heat transfer intensification during flow boiling in mini-channels. Therefore, during the experimental sets, the heated plate was replaced. In specific experimental sets, the plate surface in contact with the fluid in the mini-channels was modified in four processes: electro-machining texturing [14,15], laser surface texturing [15], by iron powder soldering to the base plate (resulting in a porous structure forming) [14,16,17] or by using emery papers of four varying roughnesses (P-36, P-80, P-220, P-389). Photographs, 3D views and roughness profiles of applied heated plate surfaces, including smooth, are presented in Figures 3–5, respectively.

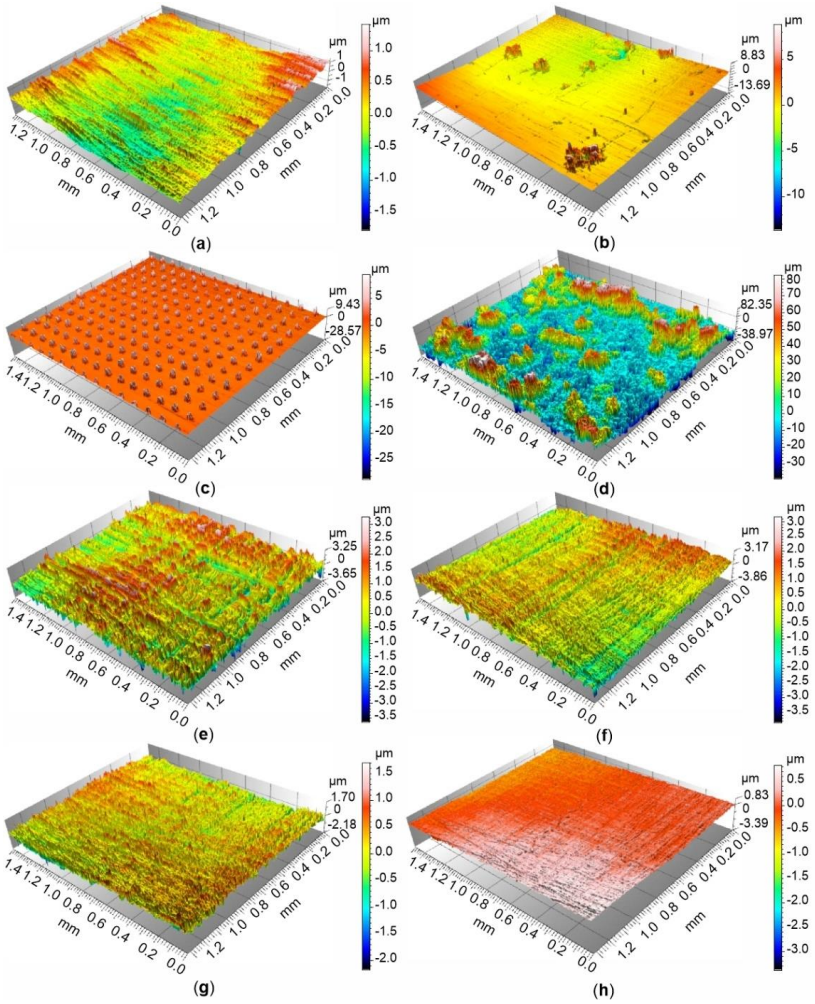

Figure 3. 3D views of the heated plate surfaces: (**a**) smooth surface, (**b**–**h**) modified surfaces developed by: electro-machining texturing (**b**), laser surface texturing (**c**), porous surface produced by soldering iron powder to the base plate (**d**) and (**e**–**h**) using emery papers of varying roughness: P-36 (**e**), P-80 (**f**), P-220 (**g**), P-389 (**h**).

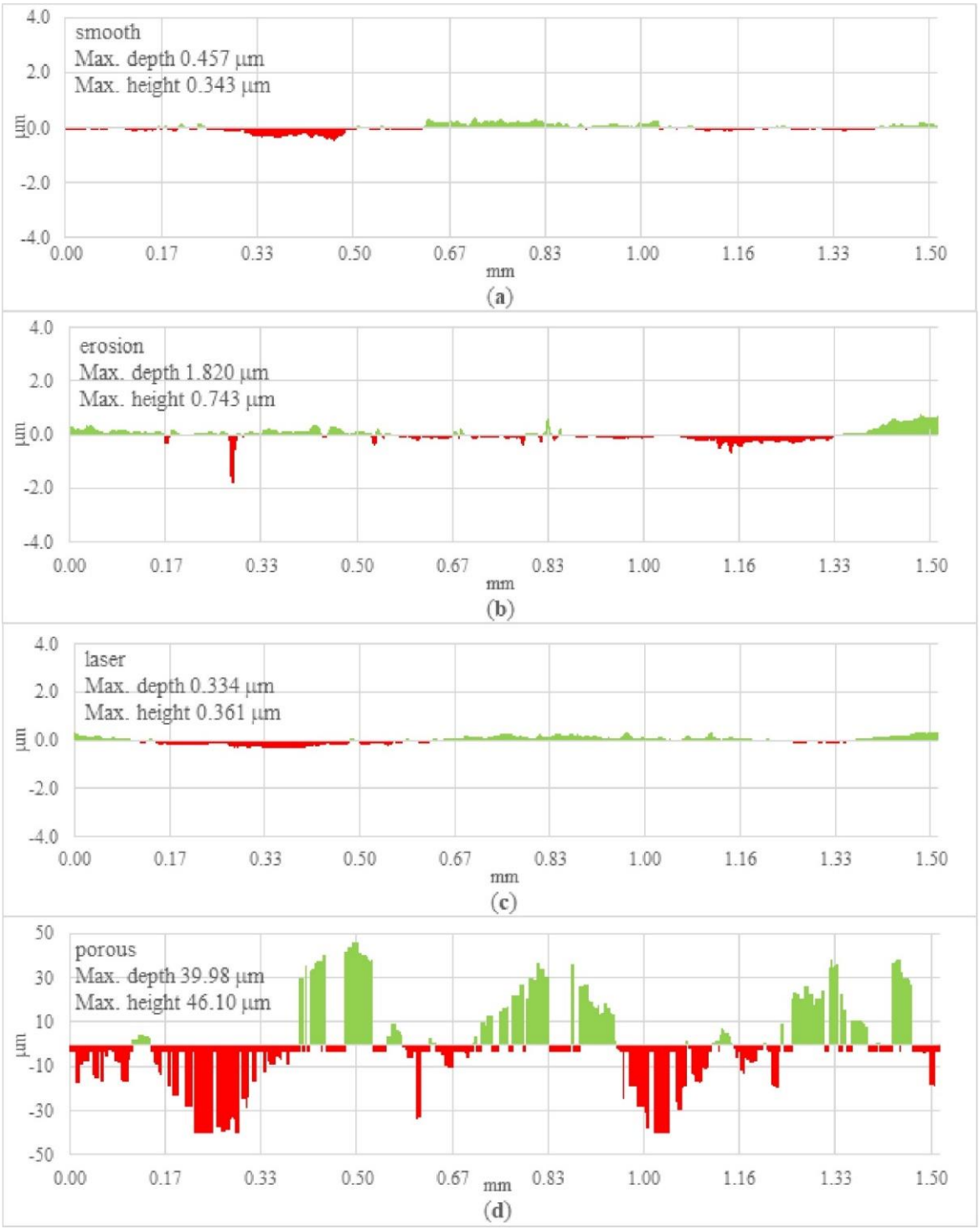

Figure 4. Topographies of the heated plate surfaces: (**a**) smooth surface, (**b**–**d**) modified surfaces developed by: electro-machining texturing (**b**), laser surface texturing (**c**) and porous surface produced by soldering iron powder to the base plate (**d**); green points mean the data which achieve values higher than the reference level, and the red points—values lower than the reference level.

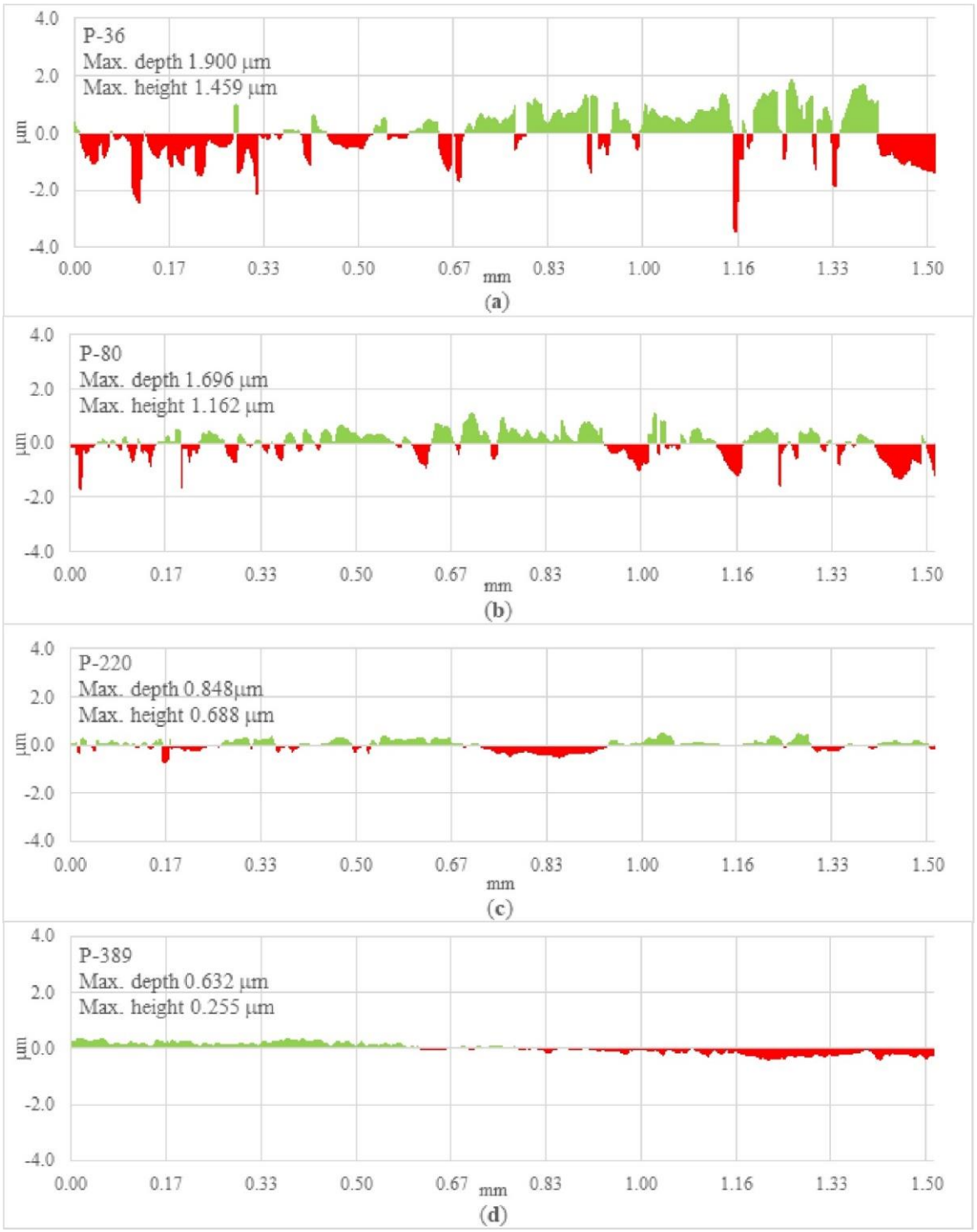

Figure 5. Topographies of the heated plate surfaces produced by using emery papers of various roughnesses: P-36 (**a**), P-80 (**b**), P-220 (**c**) and P-389 (**d**); green points mean the data which achieve values higher than the reference level, and the red points—values lower than the reference level.

The study of the roughness parameters of the heated plate surfaces was performed at the Kielce University of Technology. Analyses of geometric structures of the tested surfaces were conducted due to the Leica DCM8 confocal microscope operating in the interferometry mode (Wetzlar, Germany). The Leica DCM8 is a combined confocal microscopy instrument with high lateral resolution and interferometry to reach subnanometer vertical resolution.

The basic parameters of the instrument are as follows: vertical resolution up to 0.1 nm with HD interferometry, four LEDs for RGB HD true-color imaging, fast and reliable digital HD confocal scanning, objectives from 1.25× up to 150× in confocal, brightfield and darkfield mode, from 10× up to 50× in interferometry mode, accuracy with open loop < 3% relative error and with closed loop < 20 nm error [24]. In Table 2, the surface and area roughness parameters of these plate surfaces are listed.

Table 2. The basic data of surface roughness and area roughness parameters of the tested surfaces.

Type of the Heated Plate Surface	Roughness Parameters (μm)			
	Surface Roughness		Area Roughness	
	Ra *	***Rz*** **	***Sa*** ***	***Sz*** ****
Smooth	0.0353	0.2256	0.2683	3.1830
Electro-machining texturing	0.0747	0.8367	1.0570	22.5200
Laser surface texturing	0.0426	0.2621	0.5581	38.0000
Porous surface produced by soldering iron powder	10.8600	45.8900	15.5900	121.3000
P-36 emery paper	0.3828	2.4060	0.7099	6.8990
P-80 emery paper	0.3043	1.9480	0.6622	7.0340
P-220 emery paper	0.1536	0.8548	0.2711	3.8830
P-389 emery paper	0.0389	0.2271	0.2109	4.2180

* *Ra*—arithmetic mean deviation of the roughness profile. ** *Rz*—maximum height of the roughness profile. *** *Sa*—arithmetic mean height of surface roughness. **** *Sz*—maximum height of surface roughness.

According to the data presented in Figure 3, Figure 4, Figure 5 and Table 2, it can be seen that the highest depth and height were achieved on the modified surface for the porous structure produced by the iron powder soldering to the base plate (max. depth of 39.98 μm, max. height 46.10 μm, Figure 4) while the roughness profile and the surface roughness parameters prove the following roughness values: *Ra* = 10.86 μm, *Sa* = 15.59 μm (Table 2). Furthermore, higher values were obtained for the electro-machining textured surface (max. depth 1.82 μm, max. height 0.743 μm, Figure 4), *Ra* = 0.0747 μm, *Sa* = 1.057 μm (Table 2) and produced using P-36 emery paper (max. depth 1.90 μm, max. height 1.459 μm, Figure 5), *Ra* = 0.3828 μm, *Sa* = 0.7099 μm (Table 2). Definitely the smallest surface development and the smallest depth and height were achieved for laser surface texturing (max. depth 0.334 μm, max. height 0.361 μm, Figure 4), *Ra* = 0.0426 μm, *Sa* = 0.5581 μm (Table 2) and produced with P-389 emery paper (max. depth 0.632 μm, max. height 0.255 μm, Figure 5), *Ra* = 0.0389 μm, *Sa* = 0.2109 μm (Table 2).

4. The Heat Transfer Coefficient

4.1. Calculations

The central mini-channel of the test section was taken into account as a model channel in further considerations. The heat transfer coefficient between the heated plate and the flowing fluid was calculated using the one-dimensional mathematical method. In this method, the assumption of the only heat transfer direction (x) consistent with the depth of the thickness of the mini-channel and the heated plate was considered.

Local heat transfer coefficients $\alpha(x)$ at the subcooled and saturated boiling regions were determined from the following dependence:

$$\alpha(x) = \frac{q_w - q_{loss}}{\left(T_{IRT} - T_f(x) - q_w \cdot \frac{\delta_P}{\lambda_P}\right)} \quad (1)$$

where:

x is the coordinate consistent with the direction along the flow; q_w is the heat flux transferred to the fluid in the mini-channel while $q_w = \frac{I \cdot \Delta U}{A}$, similar to [14], I—current supplied to the heated plate (measured), ΔU—the voltage drop across the heated plate (measured), A—the surface area of the heated plate and q_{loss} means heat loss to the surroundings;

T_{IRT} is the local temperature of the heated plate measured on its outer surface using an infrared camera, while δ_P is the thickness of the heated plate;

$T_f(x)$ means local fluid temperature determined: (i) in the subcooled boiling from the assumption of the linear distribution of the fluid temperature along the mini-channel (fluid temperature measurements at the inlet and the outlet) or (ii) in the saturated boiling temperature, calculated on the basis of the liquid saturated temperature dependent on pressure (fluid pressure measurements at the inlet and the outlet);

λ_P is the coefficient of thermal conductivity of the heated plate (Haynes-230), according to its manufacturer.

The heat loss to the surroundings q_{loss} usually amounts to a few percent, for example, in [14] it was equal to 1.3% of the imposed heat flux. The heat loss to the surrounding values was determined according to the dependence

$$q_{loss} = a_s(T_{IRT} - T_a) \tag{2}$$

where: a_s—the heat transfer coefficient at the interface between the heated plate and the surroundings and T_a—ambient temperature.

Maximum values of the heat loss to the surroundings calculated from Equation (2) are listed in Table 3.

Table 3. Maximum values of the heat loss to the surroundings' q_{loss}.

Experiments with Upward Flow		Experiments with Downward Flow	
Type of the Heated Plate Surface	q_{loss} **(%)**	**Type of the Heated Plate Surface**	q_{loss} **(%)**
Smooth	0.92	Smooth	1.15
Erosion	1.04	Erosion	1.12
Laser	1.45	Laser	1.35
Porous	1.66	Porous	1.11
P-36	1.25	P-36	0.97
P-80	0.83	P-80	0.85
P-220	1.88	P-220	1.98
P-389	0.86	P-389	0.85

The average value of the maximum errors of heat loss to the surroundings calculated on the basis of experiments with fluid upward flow equals 1.24%. For a downward flow, the value of 1.17% was obtained.

4.2. The Mean Relative Error Determination

The mean relative error σ_α of the heat transfer coefficient was calculated from the following formula:

$$\sigma_\alpha = \frac{\sqrt{\left(\frac{\partial\alpha(x)}{\partial T_{IRT}(x)}\Delta T_{IRT}(x)\right)^2 + \left(\frac{\partial\alpha(x)}{\partial T_f(x)}\Delta T_f(x)\right)^2 + \left(\frac{\partial\alpha(x)}{\partial\lambda_P}\Delta\lambda_P\right)^2 + \left(\frac{\partial\alpha(x)}{\partial\delta_P}\Delta\delta_P\right)^2 + \left(\frac{\partial\alpha(x)}{\partial q_w}\Delta q_w\right)^2}}{\alpha(x)} \tag{3}$$

The components of the mean relative error of the heat transfer coefficient assumed in the calculation are shown in Table 4.

The lowest value of the heat flux supplied to the heated plate was selected in the subcooled boiling region (q_w = 32.5 kW/m^2) and in the saturated region (q_w = 54.2 kW/m^2) for the mass flux 566 kg/(m^2 s) to determine the absolute error of the heat flux Δq_w. The procedure for determining absolute and relative errors of the heat flux and assumptions was made similarly to that in [13]. The absolute error of the heat flux and relative errors of the heat transfer coefficient at the subcooled and saturated boiling regions and for upward and downward flow are listed in Table 5.

Table 4. The components assumed in the calculation of the heat transfer coefficient mean relative error σ_α.

Component of the Heat Transfer Coefficient Mean Relative Error σ_α	Absolute Error
Plate temperature measurement by infrared thermography	$\Delta T_{IRT}(x) = 2.0$ K
Fluid temperature measurement by K-type thermocouple	$\Delta T_f(x) = 0.34$ K
Thermal conductivity of the Haynes-230 (the heated plate)	$\Delta\lambda_P = 0.1$ W/(m·K)
Thickness of the heated plate	$\Delta\delta_P = 5 \times 10^{-5}$ m
Current intensity (supplied to the heated plate)	$\Delta I = 0.18$ A
Voltage drop (across the heated plate)	$\Delta(\Delta U) = 0.02$ V
Area of the heated plate	$\Delta A = 2.8 \times 10^{-5}$ m^2

Table 5. The mean relative errors of the heat flux q_w (%) and the heat transfer coefficient σ_α (%) at the subcooled and saturated boiling regions for upward and downward flows.

Upward Flow					
Subcooled Boiling Region			**Saturated Boiling Region**		
Type of the Surface	q_w (%)	σ_α (%)	**Type of the Surface**	q_w (%)	σ_α (%)
Smooth	0.83	5.41	Smooth	0.77	31.40
Erosion	0.91	5.05	Erosion	0.74	29.26
Laser	0.96	5.19	Laser	-	-
Porous	0.97	4.66	Porous	3.81	13.89
P-36	0.80	5.20	P-36	3.32	15.43
P-80	0.80	5.05	P-80	3.56	15.94
P-220	0.99	5.21	P-220	3.81	21.44
P-389	0.82	5.32	P-389	3.36	10.39
Downward Flow					
Subcooled Boiling Region			**Saturated Boiling Region**		
Type of the Surface	q_w (%)	σ_α (%)	**Type of the Surface**	q_w (%)	σ_α (%)
Smooth	0.83	5.48	Smooth	0.71	23.10
Erosion	0.92	5.70	Erosion	0.75	22.38
Laser	0.96	5.48	Laser	-	-
Porous	1.05	5.73	Porous	3.94	13.23
P-36	0.81	5.05	P-36	3.15	18.00
P-80	0.80	5.31	P-80	3.34	10.07
P-220	1.03	5.67	P-220	3.41	9.75
P-389	0.80	5.37	P-389	3.48	13.81

When analyzing the results, it was noticed that the absolute error of the heat flux was at most a few percent, in the range 0.71–3.94%. In the case of the mean relative error of the heat transfer coefficient, the results achieved for the subcooled boiling region were much lower than those obtained in the saturated boiling region, as mentioned in earlier works [13,25]. The relative errors of the heat transfer coefficient were in the range of 4.66–5.73% in the subcooled boiling region and 9.75–31.4% in the saturated boiling region. The mean relative error of the coefficient for the subcooled boiling region was $\sigma_\alpha = 5.3\%$ and for the saturated boiling region $\sigma_\alpha = 17.7\%$.

5. Experiments, Results and Discussion

Before target experiments, degasification of the working fluid in the circulating loop was provided, and the mass flow rate, liquid pressure and temperature at the mini-channels inlet were adjusted. Laminar flow of the working fluid occurred in the mini-channels. After stabilizing these experimental parameters, the current was supplied to the heated plate.

When the boiling process starts, the subcooled boiling region occurs. It is worth underlining that in this region the fluid is subcooled in the core of the flow and in the

vicinity of the heated plate it is superheated. Afterwards, with increases in the imposed heat flux, in the temperature of the heated wall and fluid, the temperature of the heated wall and fluid subsequently increased, and the saturated boiling region took place (it is assumed that when the difference between temperatures of the heated wall and the saturation temperature is higher than zero the saturated boiling region occurs).

The series of experiments were conducted in the steady state under similar thermal and flow conditions. The main characteristics of the selected experiments are shown in Figure 6. As is clearly shown, in addition to the use of various types of heated plate surface, two vertical channel positions were applied, two values of mass flux were set and six values of the heat flux were chosen for analysis.

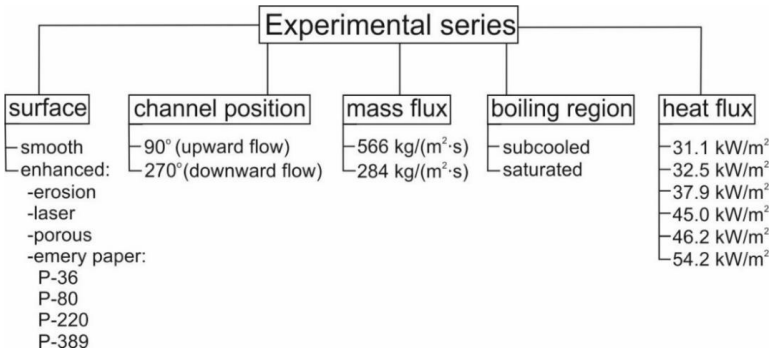

Figure 6. Main characteristics of the experimental series.

It should be added that the temperature of the heated plate, measured on the outer surface plate due to the infrared camera, was based on the distribution of recorded color on the examined surface. The data used in the calculation were collected on the smooth surface of the heated plate side, which was covered with black paint (of known emissivity of 0.97), along the central line in the axially symmetric part of the central mini-channel.

In general, the results are shown in Figures 7–16. In parts 'a' and 'c' of Figures 7–12, the data obtained on the basis of experiments with enhanced surfaces received with the use of emery paper characterized by four sizes of grit (P-36, P-80, P-220 and P-389) are revealed. Moreover, in parts 'b' and 'd' of these figures and Figures 14a,b and 15a,b, the results are illustrated for a smooth surface of the heated plate and modified in various processes, that is, produced by electro-machining texturing, laser surface texturing, surface formed with the use of emery paper (selected for the term of achieving high values of the heat transfer coefficient, based on the results shown in the previous graphs) and porous surface produced by soldering iron powder to the base plate, to compare all the results. In Figures 13, 14c,d and 15c,d, data for two enhanced surfaces (produced by electro-machining and laser texturing) and one smooth surface are presented.

In detail, the results are presented in the following forms:

- The temperature of the heated plate measured by an infrared as a function of the distance from the mini-channel inlet, for two vertical test section orientations: with upward flow 90° (Figures 7a,b, 8a,b and 9a,b) and with downward flow 270° (Figures 7c,d, 8c,d, 9c,d and 13a–c); the results concern mass flux of 566 kg/(m^2·s) (Figures 7–9) or 284 kg/(m^2·s) (Figure 13a–c) and six values of the heat flux: two chosen in the subcooled boiling region (32.5 kW/m^2 and 46.2 kW/m^2 (Figures 7 and 8)) and four in the saturated boiling region (54.2 kW/m^2 (Figure 9), 31.1 kW/m^2, 37.9 kW/m^2 and 45.0 kW/m^2 (Figure 13a–c));
- The heat transfer coefficient versus distance from the mini-channel inlet, for two vertical test section orientations: with upward flow 90° (Figures 10a,b and 11a,b) and with downward flow 270° (Figures 10c,d and 11c,d)—the results for the subcooled boiling region, corresponding to the temperature of the heated plate presented in previous graphs;

- The heat transfer coefficient versus distance from the mini-channel inlet, for two vertical test section orientations: with upward flow 90° (Figure 12a,b) and with downward flow 270° (Figures 12c,d and 13d–f)—the results for the saturated boiling region, corresponding to the temperature of the heated plate presented in previous graphs;
- Boiling curves—the heat flux as a function of the temperature of the heated wall and fluid difference, generated two distances from the mini-channel inlet: 0.011 m (Figure 14) and 0.021 m (Figure 15); for two vertical test section orientations and two values of mass flux, i.e., 566 kg/(m^2·s) and 284 kg/(m^2·s), while the heated plate surface in contact with the fluid was smooth and developed by electro-machining and laser surface texturing;
- Images of two-phase flow structures (Figure 16), collected for two vertical test section orientations: with upward flow 90° (Figure 16a–c) and downward flow 270° (Figure 16d–f); for mass flux of 284 kg/(m^2·s) while the heated plate surface in contact with the fluid was smooth and developed by electro-machining and laser surface texturing;
- The results of the temperatures and heat transfer coefficients—presented in Tables 6 and 7, for the subcooled and saturated boiling regions, respectively.

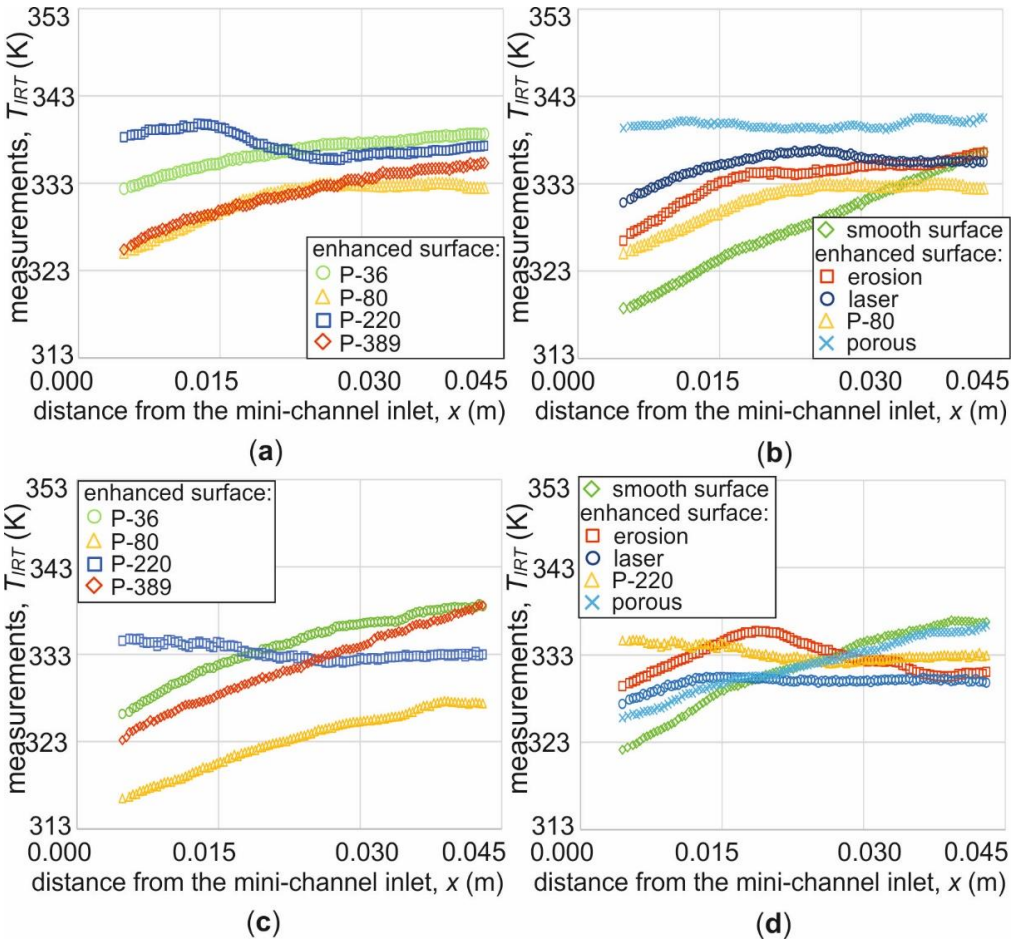

Figure 7. The temperatures of the heated plates measured by an infrared camera versus distance from the mini-channel inlet, for two vertical test section orientations: with upward flow 90° (**a**,**b**) and downward flow 270° (**c**,**d**); the subcooled boiling region; experimental data: mass flux of 566 kg/(m^2·s); heat flux q_w = 32.5 kW/m^2; the heated plate surface in contact with the fluid, smooth and developed by: electro-machining texturing (erosion), laser surface texturing (laser), porous surface produced by soldering iron powder (porous), produced with the use of emery papers of varying roughness: P-36, P-80, P-220, P-389.

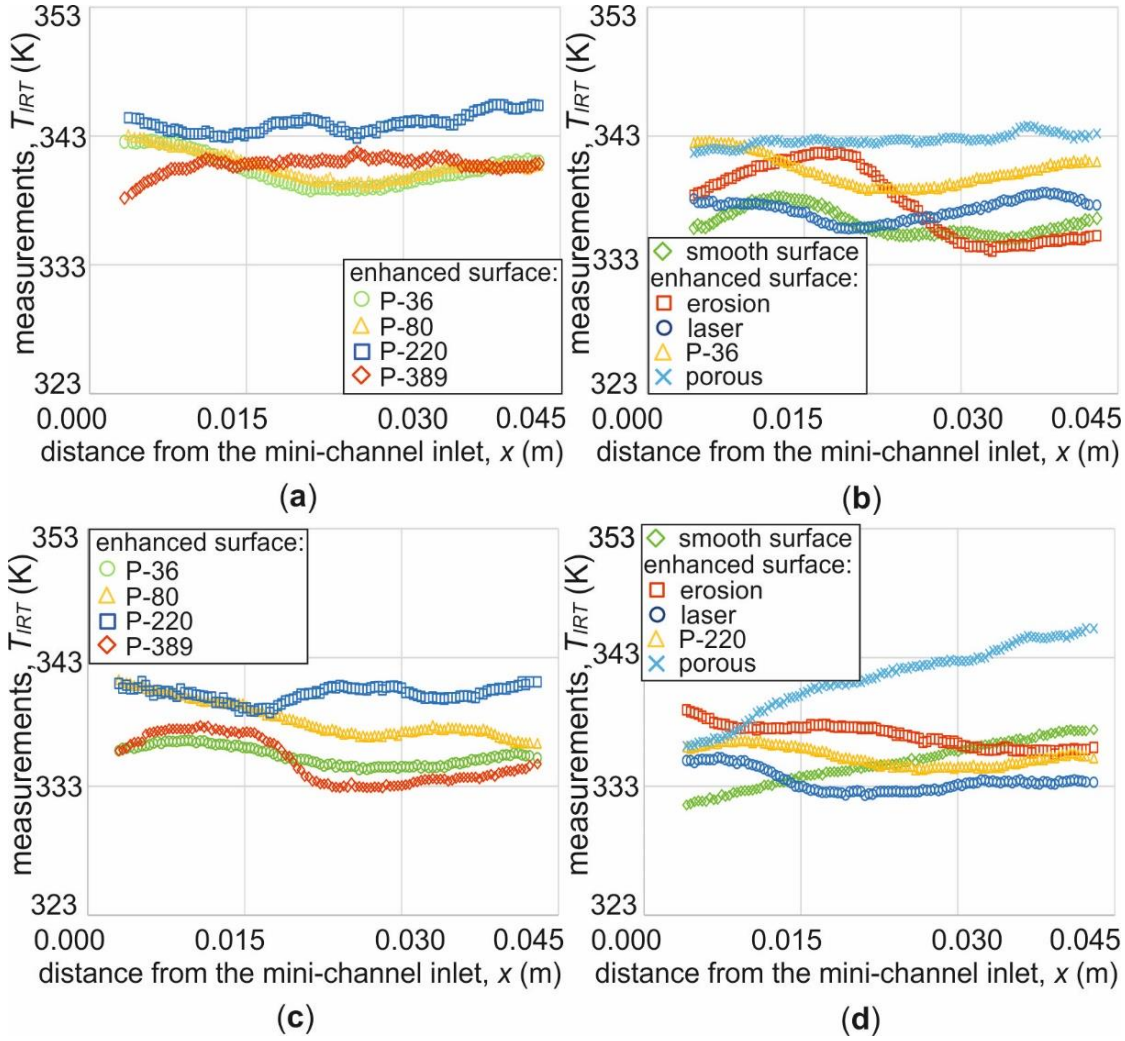

Figure 8. The temperature of the heated plate measured by an infrared camera versus distance from the mini-channel inlet, for two vertical test section orientations: with upward flow 90° (**a**,**b**) and downward flow 270° (**c**,**d**); the subcooled boiling region; experimental data: mass flux of 566 kg/(m^2·s); heat flux q_w = 46.2 kW/m^2; the heated plate surface in contact with the fluid: smooth and developed by: electro-machining texturing (erosion), laser surface texturing (laser), porous surface produced by soldering iron powder (porous), produced with the use of emery papers of varying roughness: P-36, P-80, P-220, P-389.

According to the data presented in Figure 7, it can be seen that for the subcooled boiling region and the lower heat flux, while taking into account the modified surfaces due to the use of emery paper, for both vertical positions of the test section, the highest values of the heated plate temperature were achieved for P-36 and P-220 (Figure 7a,c), but the lowest was noticed for P-80. Compared to the data collected for all selected surfaces, it is obvious that the porous surface gave the highest temperature, while for the smooth surface the lowest temperature occurred for the upward flow (Figure 7b). Furthermore, in the subcooled boiling region, at a higher value of heat flux, it can also be observed that the highest heated plate temperature was achieved for P-220, of all surfaces produced using emery papers (Figure 8a,c). Taking into account all surfaces examined, the use of the porous one in the experiments caused the highest temperature of the heated wall (Figure 8b,d). The observations concerning the lowest temperatures of the heated wall in relation to the roughness of the heated wall are not unequivocal. More detailed comments are provided in Table 6.

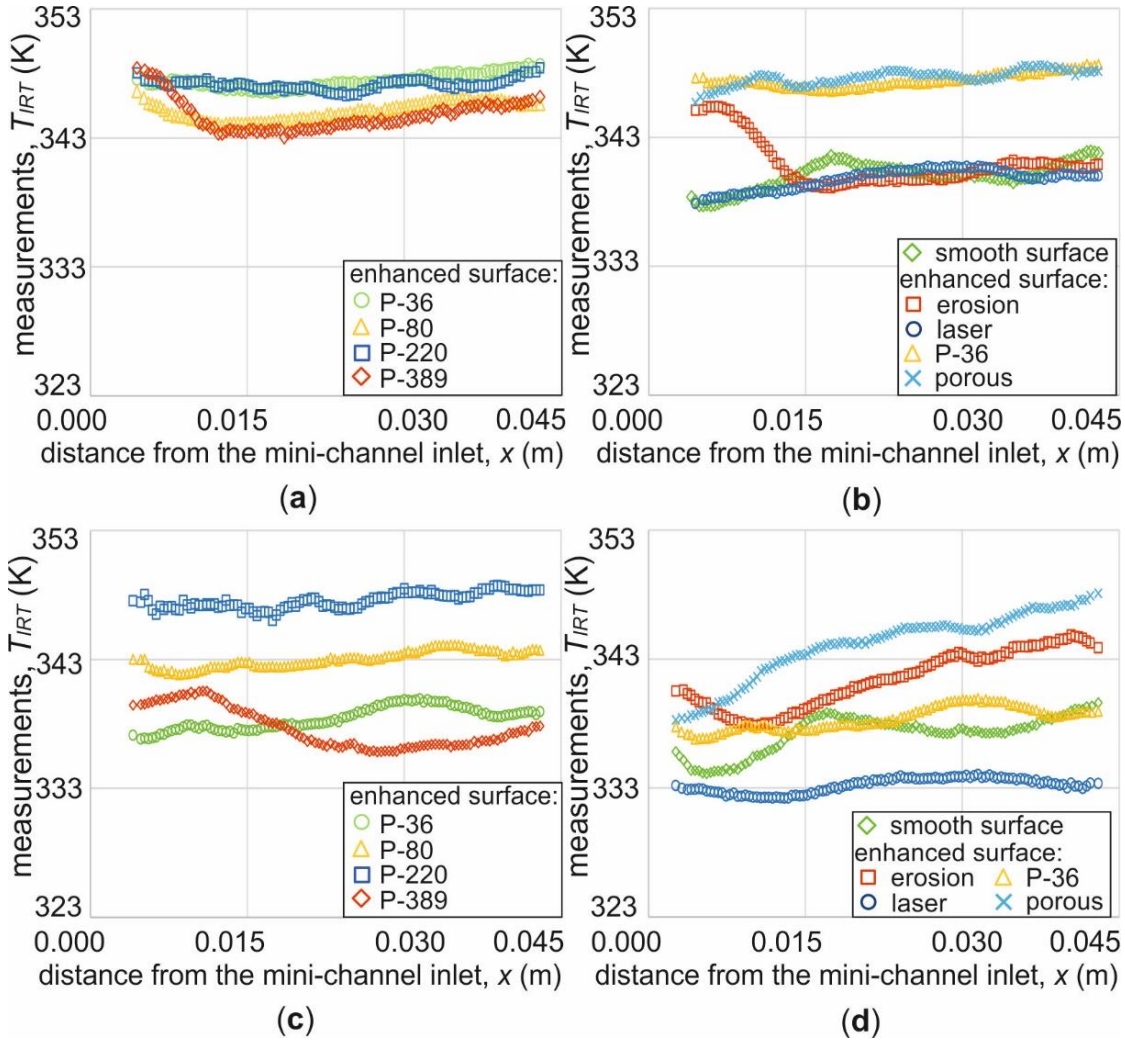

Figure 9. The temperature of the heated plate measured by an infrared camera versus distance from the mini-channel inlet, for two vertical test section orientations: with upward flow 90° (**a**,**b**) and downward flow 270° (**c**,**d**); the saturated boiling region; experimental data: mass flux of 566 kg/(m^2·s); heat flux q_w = 54.2 kW/m^2; the heated plate surface in contact with the fluid: smooth and developed by: electro-machining texturing (erosion), laser surface texturing (laser), porous surface produced by soldering iron powder (porous), produced with the use of emery papers of varying roughness: P-36, P-80, P-220, P-389.

When analyzing the data for saturated boiling shown in Figure 9, taking into account the modified heated surfaces obtained by using emery papers, it can be indicated that the highest values of the heated plate temperature for both positions of the test section were achieved for P-220 (Figure 9a,c), but only regarding upward flow: for P-36 (Figure 9a). Furthermore, when the porous surface was applied, the highest temperatures were recorded (Figure 9b,d). These findings are similar to those for the subcooled boiling region. The observations are supplemented with the note that the lowest temperatures were gained for laser surface texturing, for downward flow, in comparison to the results collected for all selected surfaces in the saturated boiling region. More comments can be found in Table 7.

It could be emphasized that the main observations regarding the heated wall temperature and the heat transfer coefficient are listed in Tables 6 and 7: in the subcooled boiling region (Table 6) and in the saturated boiling region (Table 7).

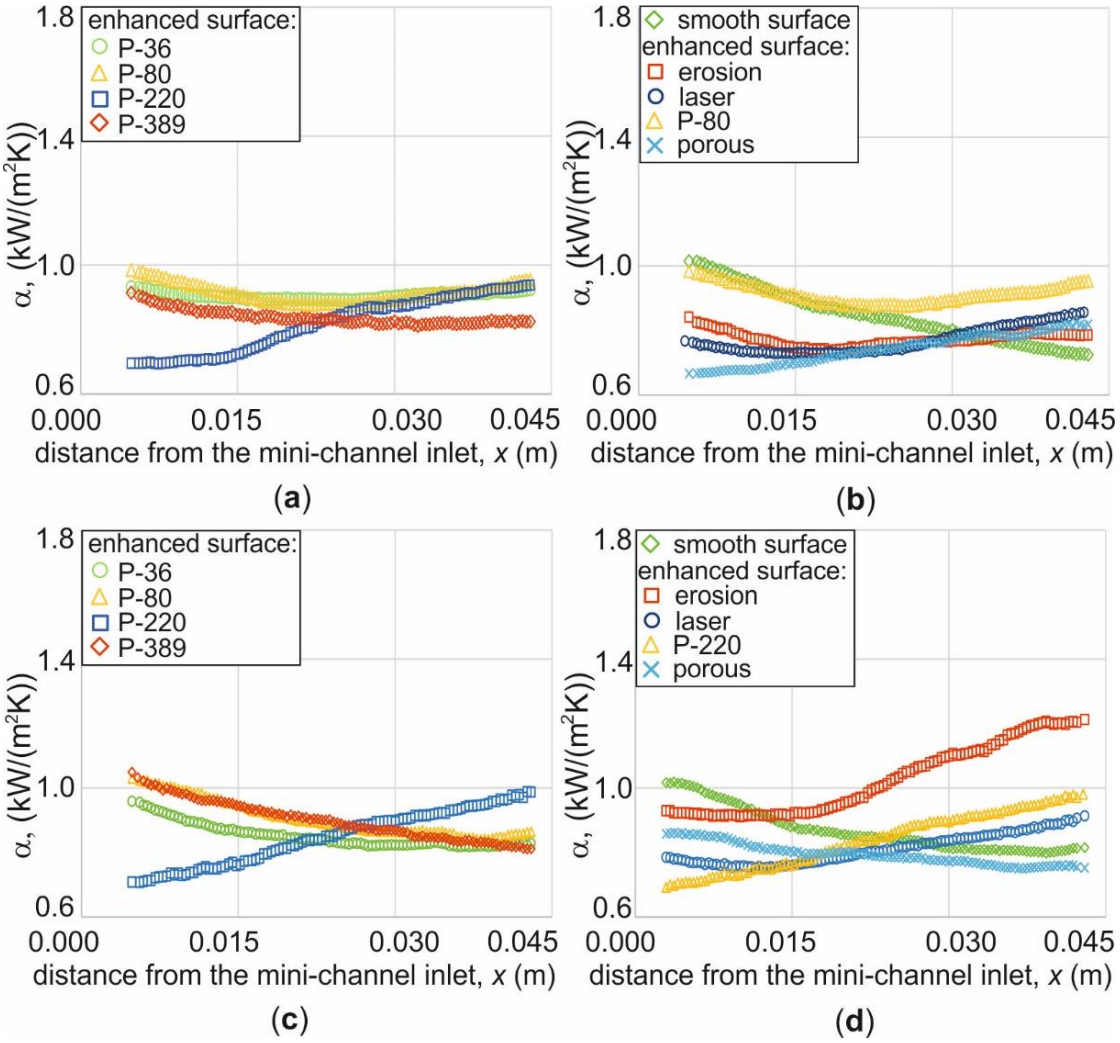

Figure 10. The heat transfer coefficient versus distance from the mini-channel inlet, for two vertical test section orientations: with upward flow 90° (**a**,**b**) and downward flow 270° (**c**,**d**); the subcooled boiling region; experimental data: mass flux of 566 kg/(m^2·s); heat flux q_w = 32.5 kW/m^2; the heated plate surface in contact with the fluid: smooth and developed by: electro-machining texturing (erosion), laser surface texturing (laser), porous surface produced by soldering iron powder (porous), produced with the use of emery papers of varying roughness: P-36, P-80, P-220, P-389.

The local heat transfer coefficients were calculated according to Equation (1). Separate coefficient plots were for the subcooled boiling region (Figures 10 and 11) and the saturated boiling region (Figures 12 and 13d–f).

When analyzing the dependences shown in Figure 10, presented as an example for the subcooled boiling region with the imposed heat flux of q_w = 32.5 kW/m^2, it can be seen that the distribution of the heat transfer coefficient with trends monotonically or decreasing in function differs in the inlet and outlet parts of the channel for various surfaces and channel orientations. Furthermore, the values of the heat transfer coefficient change to a small extent from the range 0.6–1.2 kW/(m^2 K). A more detailed remark, according to Figure 10a,b, is that for the mini-channel orientation of 90°, for all the roughnesses of the plate surface, the highest coefficient was reached for the surface produced by the P-80 emery paper. Furthermore, the highest heat transfer coefficient was achieved for 270° orientation, while the enhanced surface produced by the electro-machining texturing was applied in experiments (see Figure 10d). Other comments on the values of the heat transfer coefficient depending on channel orientation and type of surface roughness are revealed in Table 7.

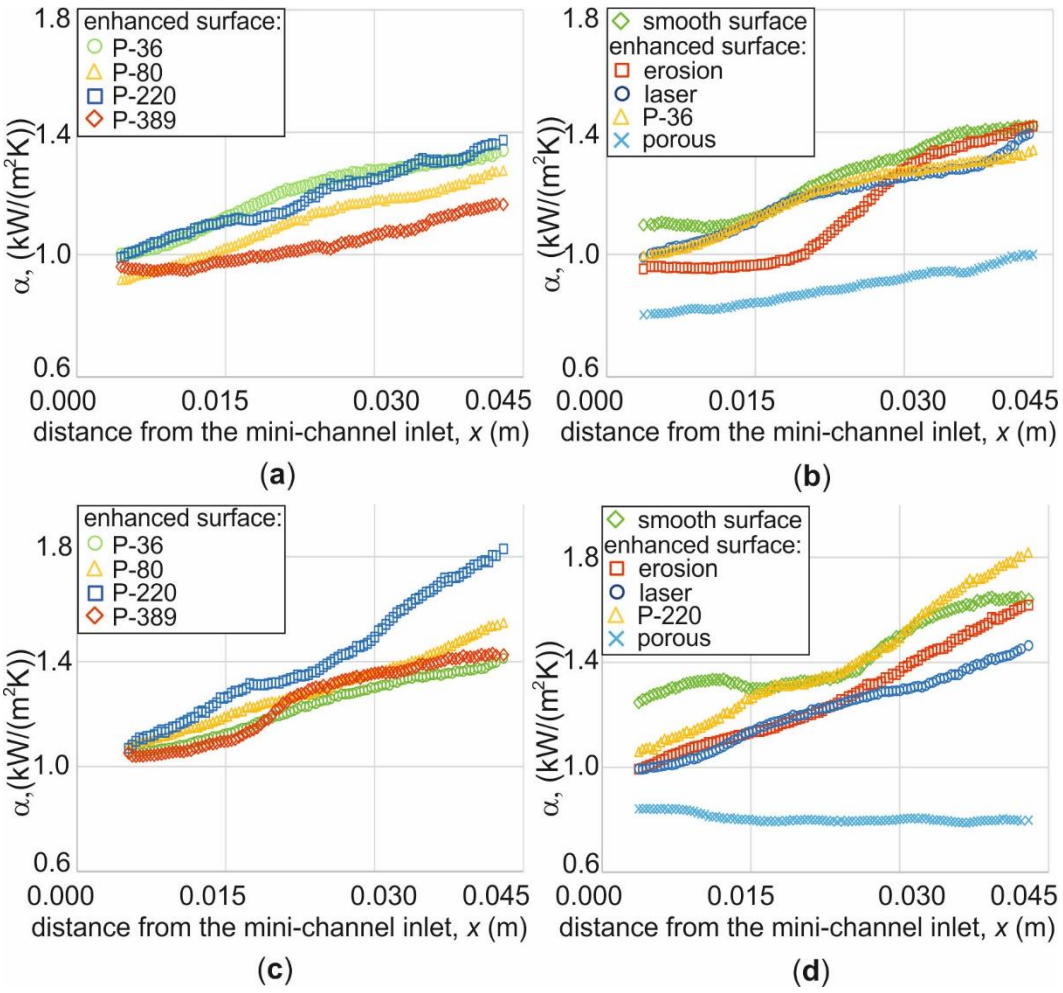

Figure 11. The heat transfer coefficient versus distance from the mini-channel inlet, for two vertical test section orientations: with upward flow 90° (**a**,**b**) and downward flow 270° (**c**,**d**); the subcooled boiling region; experimental data: mass flux of 566 kg/(m^2·s); heat flux q_w = 46.2 kW/m^2; the heated plate surface in contact with the fluid: smooth and developed by: electro-machining texturing (erosion), laser surface texturing (laser), porous surface produced by soldering iron powder (porous), produced with the use of emery papers of varying roughness: P-36, P-80, P-220, P-389.

The results shown in Figure 11 were also obtained in the subcooled boiling region, but for a higher heat flux compared to the data presented in Figure 10. In general, the heat transfer coefficient increases with increasing distance from the mini-channel inlet. The local heat transfer coefficients were significantly higher than those determined for q_w = 32.5 kW/m^2 and were in the range of 0.9 to 1.9 kW/(m^2 K) for all surfaces tested, except the porous one (see Figure 11b,d). The use of a porous surface produced by soldering iron powder in experiments caused the heat transfer coefficient to reach the lowest values compared to other surfaces. Furthermore, it can be observed that the heat transfer coefficient calculated from the data from the experiments with the use of P-220 emery paper in the production of enhanced heated surfaces achieved mostly the highest values compared to those obtained for other surfaces produced in similar surface roughness (see Figure 11a,c,d). It can be explained that in Figure 11b (dedicated to the 90° orientation of the test section) the results obtained for P-220 are not illustrated. The reason is that the data collected for P-36 and P-220 achieved similar and highest values compared to other surfaces produced with the use of emery papers, but only P-36 was included in the further analysis as it performed slightly better in the heat transfer coefficient results. Furthermore, more detailed comments are included in Table 6.

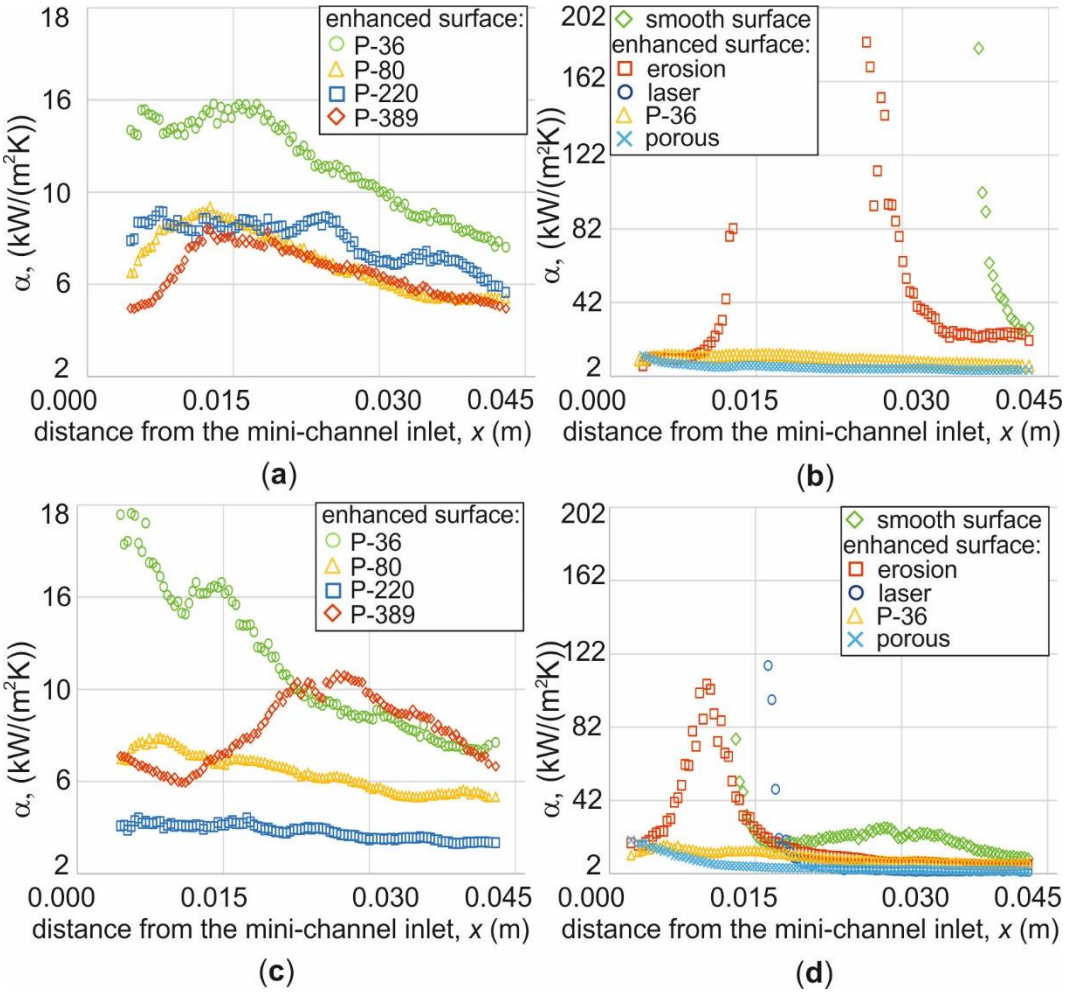

Figure 12. The heat transfer coefficient versus distance from the mini-channel inlet, for two vertical test section orientations: with upward flow 90° (**a**,**b**) and downward flow 270° (**c**,**d**); the saturated boiling region; experimental data: mass flux of 566 kg/(m^2·s); heat flux q_w = 54.2 kW/m^2; the heated plate surface in contact with the fluid: smooth and developed by: electro-machining texturing (erosion), laser surface texturing (laser), porous surface produced by soldering iron powder (porous), produced with the use of emery papers of varying roughness: P-36, P-80, P-220, P-389.

When analyzing the results for all surfaces produced due to the emery papers shown in Figure 12, it can be indicated that the highest heat transfer coefficient was achieved for P-36 (see Figure 12a,c). Furthermore, the coefficient for each 'emery surface' reached a maximum of 18 kW/(m^2 K), which is much lower compared to the results obtained for other enhanced surfaces (see Figure 12b,d). The lowest values of the heat transfer coefficient were observed for P-220, for downward flow (270°), Figure 12c. The highest coefficient compared to all tested surfaces was noticed for the electro-machining textured surface, for both channel orientations (Figure 12b,d). The laser-textured surface, set at 270°, helped achieve very high values of the heat transfer coefficient (Figure 12d). The lowest coefficient was observed for the use of a porous surface, for each channel orientation (Figure 12b,d). Other comments can be found in Table 7.

Figure 13 illustrates the results in the saturated boiling region, in the form of the temperature of the heated plate (Figure 13a–c) and the heat transfer coefficient (Figure 13d–f) as a function of the distance from the inlet, when the downward flow (270°) was established in the mini-channels. The dependences mostly confirmed previous results regarding the distribution of temperature. The results indicate a sharp increase in temperature with an increasing distance from the inlet. However, a similar dependence is shown in Figure 9d.

The highest local temperature was recorded during laser surface texture and the lowest for the use of a smooth heated surface (Figure 13a–c). Furthermore, the dependence of the heat transfer coefficient shown in Figure 13d–f indicates a sharp decrease with distance from the inlet, but the dependence shown in Figure 12d is similar only in part of the channel length. It should be underlined that the coefficient values are also much lower than those in Figure 12d, but the data in Figure 13 are obtained for lower imposed heat flux compared to the mentioned data. The highest heat transfer coefficient was obtained for electro-machining texturing and the lowest for laser texturing (Figure 13d–f).

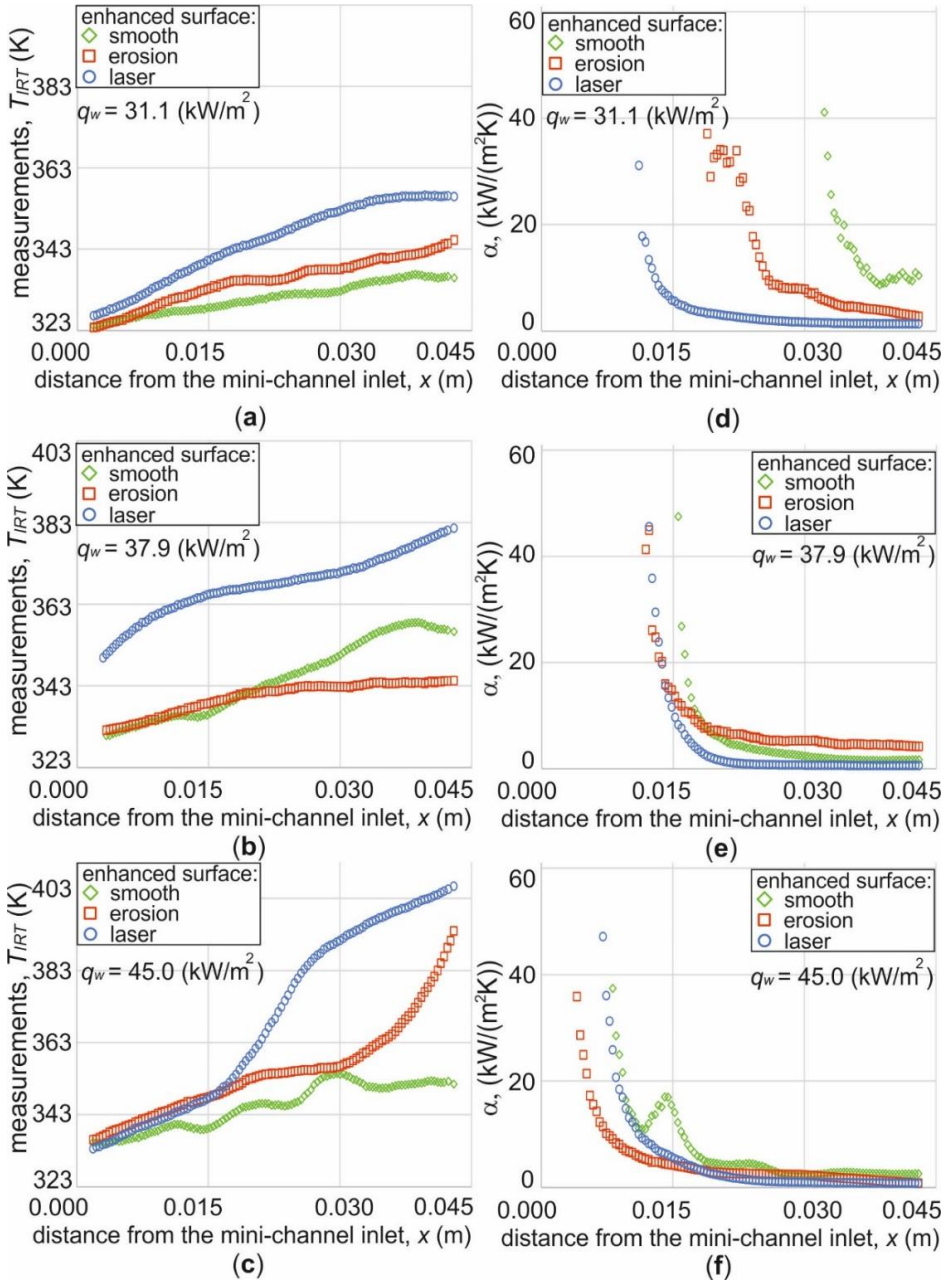

Figure 13. The temperature of the heated plate measured by an infrared camera (**a**–**c**) and the heat transfer coefficient (**d**–**f**) versus distance from the mini-channel inlet, the vertical test section with downward flow 270°; the saturated boiling region; experimental data: mass flux of 284 kg/(m^2·s); three values of the heat flux: q_w = 31.1 kW/m^2 (a,d), q_w = 37.9 kW/m^2 (b,e), and q_w = 45.0 kW/m^2 (c,f), the heated plate surface in contact with the fluid: smooth and developed by electro-machining texturing (erosion) and laser surface texturing (laser).

Table 6. Main observations concerning the results from the experiments on flow boiling in mini-channels in the subcooled boiling region.

Heat Flux q_w (kW/m^2)	Mass Flux G (kg/(m^2·s))	Orientation (°)	Heater Temperature T_{IRT} (K)	Heat Transfer Coefficient α (kW/(m^2·K))
32.5	566	90	the highest T_{IRT} (i) P-36 and P-220 (Figure 7a) (ii) porous (Figure 7b) the lowest T_{IRT} (i) P-80 and P-389 (Figure 7a) (ii) smooth (Figure 7b)	the highest α (i) P-80 (Figure 10a,b) the lowest α (i) P-220, at the inlet and P-389, at the outlet (Figure 10a) (ii) porous, at the inlet and smooth, at the outlet (Figure 10b)
		270	the highest T_{IRT} (i) P-36, at the outlet and P-220, at the inlet (Figure 7c) (ii) indecisive results, vary depending locally (Figure 7d) the lowest T_{IRT} (i) P-80 (Figure 7c) (ii) smooth, at the inlet and laser, at the outlet (Figure 7d)	the highest α (i) P-80 and P-389, at the inlet, and P-220, at the outlet (Figure 10c) (ii) erosion, except the inlet (Figure 10d) the lowest α (i) P-220, at the inlet (Figure 10c,d) and P-36, at the outlet (Figure 10c) (ii) porous, at the outlet (Figure 10d)
46.2	566	90	the highest T_{IRT} (i) P-220 (Figure 8a) (ii) porous (Figure 8b) the lowest T_{IRT} (i) P-389, at the inlet and P-36 in the central part (Figure 8a) (ii) erosion, at the outlet (Figure 8b)	the highest α (i) P-36 and P-220 (Figure 11a) (ii) smooth (Figure 11b) the lowest α (i) P-389 (Figure 11a) (ii) porous (Figure 11b)
		270	the highest T_{IRT} (i) P-220 (Figure 8c) (ii) porous, except the inlet (Figure 8d) the lowest T_{IRT} (i) P-389, at the outlet (Figure 8c) (ii) laser, except the inlet (Figure 8d)	the highest α (i) P-220 (Figure 11c) (ii) P-220, except the inlet where smooth surface is the highest (Figure 11d) the lowest α (i) P-389, at the inlet and smooth, for the rest of the entire distance (Figure 11c) (ii) porous (Figure 11d)

When analyzing all the temperature data for most experiments, an increasing tendency with increasing distance from the mini-channel inlet can be noticed. The temperatures of the results ranged from 315 K to 350 K (Figures 7–9) or from 325 K to 405 K (Figure 13a–c). It can be highlighted that the temperature of the heated plate in the subcooled boiling region was relatively low compared to that in the saturated boiling region.

In general, the heat transfer coefficients of the subcooled boiling region were relatively low compared to those of the saturated boiling region. The values of the local heat transfer coefficients increased slightly with distance from the mini-channel inlet and approximately in the range of 0.7 kW/(m^2·K) to 1.9 kW/(m^2·K) (Figures 10 and 11). It was confirmed that in the saturated boiling region, the heat transfer coefficient was very high for all enhanced heated plates, with values up to 100 times greater than those obtained for the subcooled boiling region. Similar dependencies were observed in the previous works of the authors [13,19]. The local heat transfer coefficients in the saturated boiling region were in the range of 2 kW/(m^2·K) to 200 kW/(m^2·K) (Figure 12), from 1 kW/(m^2·K) to 48 kW/(m^2·K) (Figure 13d–f).

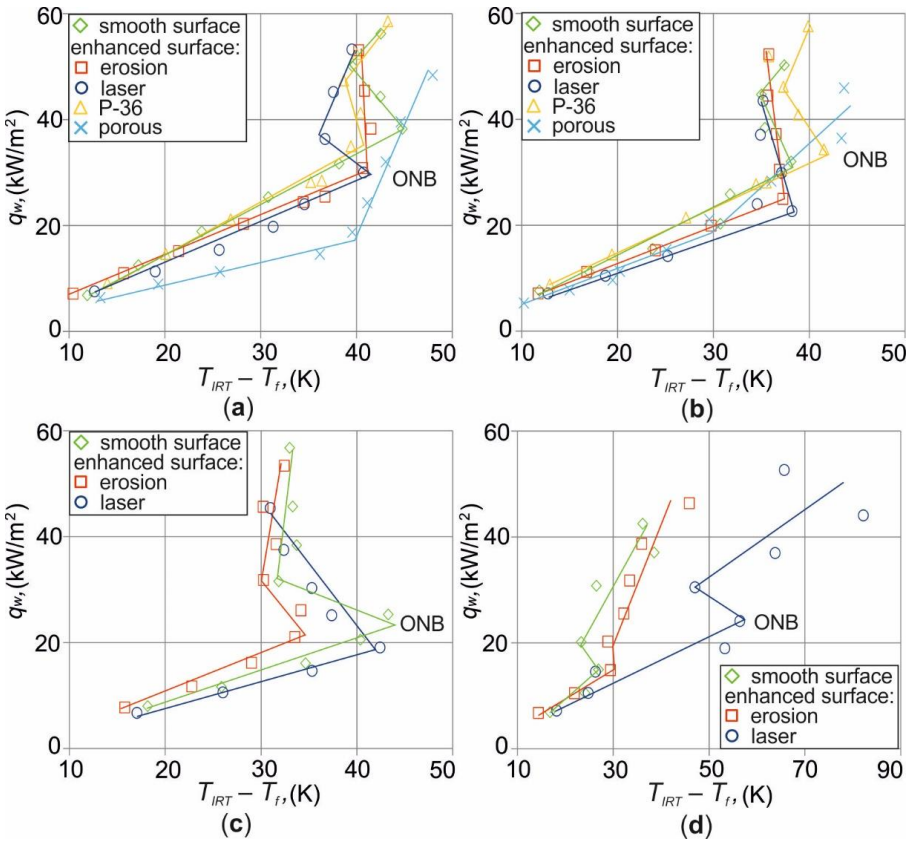

Figure 14. Boiling curves generated for 0.011 m distance from the mini-channel inlet; for two vertical test section orientations: with upward flow 90° (**a**,**b**) and downward flow 270° (**c**,**d**); mass flux of 566 kg/(m^2·s) (**a**,**b**) and 284 kg/(m^2·s) (**c**,**d**); the heated plate surface in contact with the fluid: smooth and developed by electro-machining texturing (erosion) and laser surface texturing (laser); ONB—onset of nucleate boiling.

Table 7. Main observations concerning the results from the experiments on flow boiling in mini-channels in the saturated boiling region.

Heat Flux q_w (kW/m^2)	Mass Flux G (kg/(m^2·s))	Orientation (°)	Heater Temperature T_{IRT} (K)	Heat Transfer Coefficient α (kW/(m^2·K))
54.2	566	90	the highest T_{IRT} (i) P-36 and P-220 (Figure 9a-b) (ii) P-36 and porous (Figure 9b) the lowest T_{IRT} (i) P-389, except the inlet (Figure 9a) (ii) laser, smooth and erosion (except the inlet) (Figure 9b)	the highest α (i) P-36 (Figure 12a) (ii) erosion (Figure 12b) the lowest α (i) P-80 and P-389 (Figure 12a) (ii) porous (Figure 12b)
		270	the highest T_{IRT} (i) P-220 (Figure 9c) (ii) porous, except the inlet (Figure 9d) the lowest T_{IRT} (i) P-36, at the inlet and P-389, for the rest of the entire distance (Figure 9c) (ii) laser (Figure 9d)	the highest α (i) P-36, at the inlet and P-389, for the rest of the entire distance (Figure 12c) (ii) erosion, at the inlet; laser, at the central part; and smooth, at the outlet (Figure 12d) the lowest α (i) P-220 (Figure 12c) (ii) porous (Figure 12d)

Table 7. *Cont.*

Heat Flux q_w (kW/m^2)	Mass Flux G (kg/(m^2·s))	Orientation (°)	Heater Temperature T_{IRT} (K)	Heat Transfer Coefficient α (kW/(m^2·K))
31.1 37.9 45.0	284	270	the highest T_{IRT} (i) laser, for all heat fluxes (Figure 13a–c) the lowest T_{IRT} (i) smooth (Figure 13a,c) (ii) erosion, except the inlet (Figure 13b)	the highest α (i) smooth, at the lowest q_w (Figure 13d) (ii) erosion, at the central part (Figure 13e) (iii) smooth, at the highest q_w, indecisive results (Figure 13f) the lowest α (i) laser, at the highest q_w, except the inlet (Figure 13d–f)

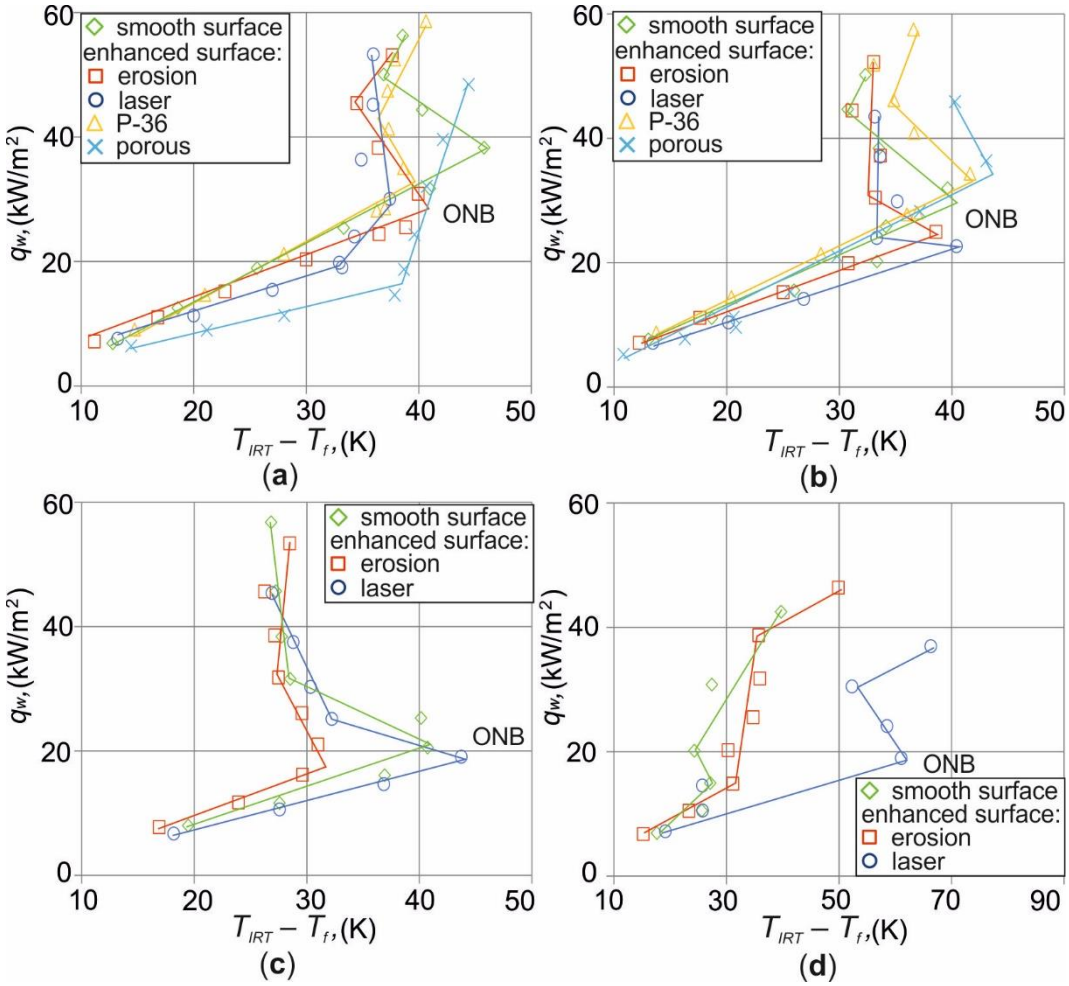

Figure 15. Boiling curves generated for 0.021 m distance from the mini-channel inlet; for two vertical test section orientations: with upward flow 90° (**a**,**b**) and downward flow 270° (**c**,**d**); mass flux of (**a**,**b**) 566 kg/(m^2·s) and (**c**,**d**) 284 kg/(m^2·s); the heated plate surface in contact with the fluid: smooth and developed by electro-machining texturing (erosion) and laser surface texturing (laser); ONB—onset of nucleate boiling.

The boiling curves were plotted for two cross-sections of the mini-channel along its central axis: 0.011 m—1/3 distance of the channel length from the channel inlet (Figure 14) and 0.021 m—1/3 distance of the channel length from the channel outlet (Figure 15), for various roughnesses of the heated plate surface (named 'smooth' and modified in different

processes). The curves represent the heat flux density as a function of the temperature difference T_{IRT} -T_f. Generally, boiling curves are typical in a shape with nucleation hysteresis, except for those obtained for porous heated surfaces (Figures 14a,b and 15a). Analysis of boiling curves courses indicates that the highest temperature differences were gained for the laser textured surface for both mass fluxes and downward flow (Figures 14c,d and 15c,d).

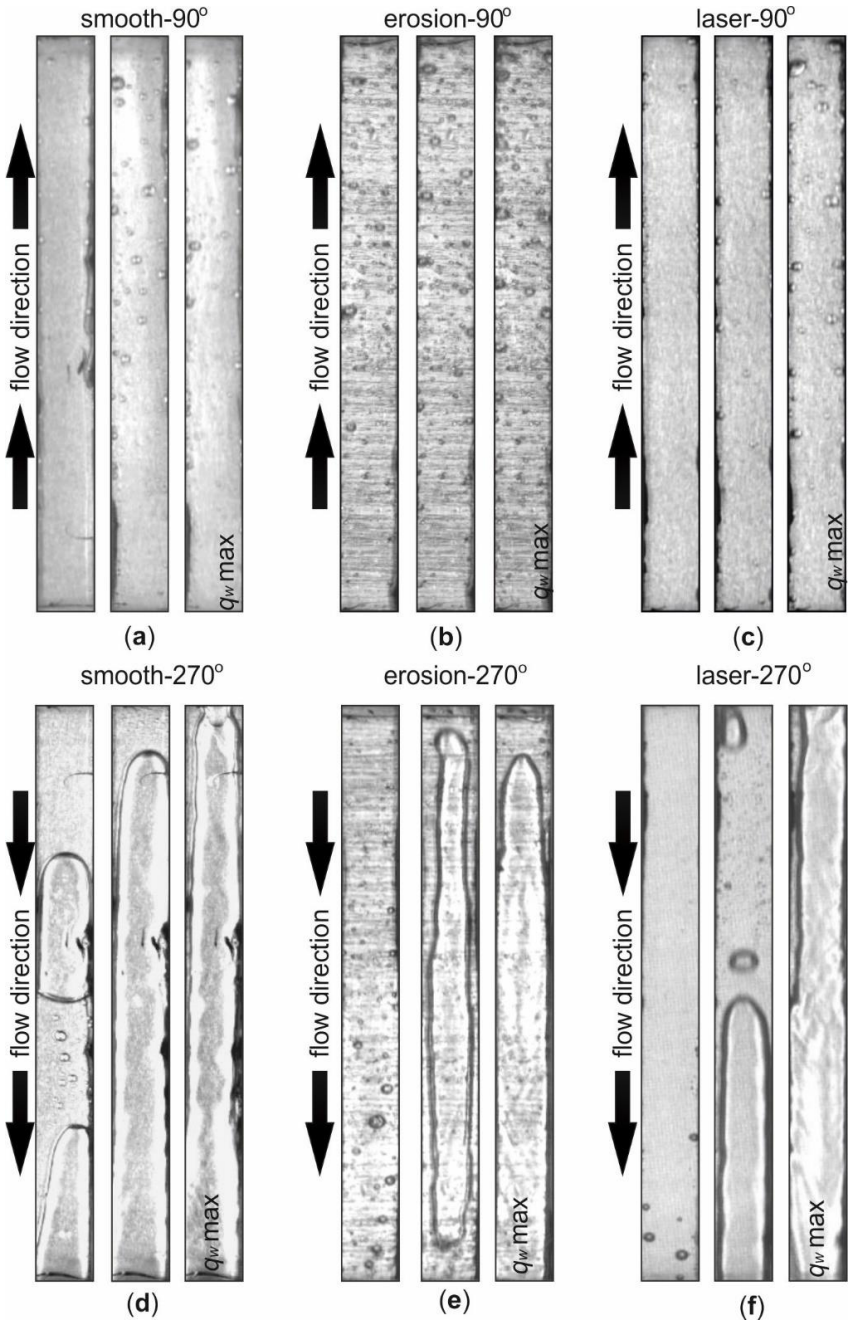

Figure 16. Images of two-phase flow structures for two vertical test section orientations: with upward flow 90° (**a**–**c**) and downward flow 270° (**d**–**f**); mass flux of 284 kg/(m^2·s); the heated plate surface in contact with the fluid: smooth and developed by electro-machining texturing (erosion) and laser surface texturing (laser).

Characteristic images of two-phase structures recorded for a mass flux of 284 kg/(m^2·s) are illustrated in Figure 16, for smooth (a,d) and modified surfaces, that is: electro-machining erosion texturing surface (b,d) and laser texturing surface (c,f). Images were

captured during an increasing of the heat flux supplied to the heated plate in upward flow (Figure 16a–c) and in downward flow (Figure 16d–f).

It was observed that in upward flow, for the smooth and laser surface, the increasing heat flux caused the formation of only single bubbly structures, but a higher number of bubbles were visible for the erosion surface (Figure 16a–c). It should be mentioned that when analyzing the heat transfer coefficient α determined for upward flow in the saturated flow boiling region when erosion plate was used in the experiments, there were higher values compared to the laser surface (Figure 13d). The analysis of the flow structures, when the enhanced heated plate surface was applied as a result of the electro-machining process, is difficult due to blurry images (the texture of the surface blurs the image). However, in downward flow, the formation of two-phase flow structures caused the transition from the bubbly to annular flow regime, which is clearly visible in the images shown at the highest heat flux (Figure 16d–f). In this flow, the two-phase flow structures that form at higher heat fluxes are characterized by a significant amount of the vapor phase in a two-phase mixture.

6. Conclusions

The main aim of this work is to present the results of experimental studies on flow boiling heat transfer along seven mini-channels 1 mm deep and 32 mm long. Steady-state experiments were performed in subcooled and saturated boiling regions. The FC-72 flowing in the mini-channels was heated by a thin plate with a modified surface. Several types of surface enhancement were tested: electro-machining texturing, laser surface texturing, iron powder soldering and produced by emery papers of four roughnesses. The temperature on the outer surface of the heater was measured by infrared thermography, while the two-phase flow patterns were recorded with a high-speed video camera. The heat transfer coefficient on the heated plate–working fluid contact surface in the central mini-channel was of particular interest. Its values were determined using the 1D mathematical method. The results were presented as the relationship between the temperature or the heat transfer coefficient and the distance along the mini-channel length, boiling curves and two-phase flow images. It was observed that when the porous heated surface was used, the highest temperature of the heated wall occurred and the lowest heat transfer coefficient was achieved. Local heat transfer coefficients in the subcooled boiling region increased with distance from the mini-channel inlet. In the saturated boiling region, the heat transfer coefficient was very high, with values up to a hundred times higher than those obtained for subcooled boiling. The highest heat transfer coefficient was obtained for electro-machining textured surfaces from all tested surfaces, but the lowest values were noticed when laser texturing was applied. The boiling curves were plotted for selected cross-sections of the mini-channel along its central axis. The highest temperature differences accompanying boiling incipience were gained for small mass fluxes and downward flow. Characteristic images of two-phase structures illustrated for upward and downward flow were demonstrated.

As a result of the investigations, it was indicated that specific micro-structed surfaces of well-defined roughness, and thermal flow parameters of work of devices and specific spatial orientation of the asymmetrically heated heat exchanger with mini-channels, could help to achieve heat transfer enhancement. More research is still needed. The results can be used in the design of compact heat exchangers with mini-channels of rectangular cross-section and variable spatial orientation.

Author Contributions: Conceptualization, M.P. and K.S.; Data curation, M.P.; Formal analysis, M.P. and K.S.; Funding acquisition, M.P.; Investigation and Methodology, M.P. and K.S.; Software, K.S.; Project administration and Supervision, M.P. and K.S.; Validation, M.P. and K.S.; Visualization, K.S.; Writing—original draft, review and editing, M.P. and K.S. All authors have read and agreed to the published version of the manuscript.

Funding: This research was funded by the National Science Centre, Poland, grant number UMO-2018/31/B/ST8/01199.

Data Availability Statement: Data sharing not applicable.

Acknowledgments: The research reported herein was supported by a grant from the National Science Centre, Poland, No. UMO-2018/31/B/ST8/01199.

Conflicts of Interest: The authors declare no conflict of interest.

Nomenclature

A	the surface area of the heated plate, m^2
a_s	heat transfer coefficient between the heated plate and surroundings, $W/(m^2 \cdot K)$
d	diameter, m
I	current, A
L	length of the channel, m
ONB	onset of nucleate boiling
p	pressure, Pa
q	heat flux, W/m^2
Ra	arithmetic mean deviation of the roughness profile, µm
Rz	maximum height of the roughness profile, µm
Sa	arithmetic mean height of surface roughness, µm
Sz	maximum height of surface roughness, µm
T	temperature, K
x	distance from the mini-channel inlet, m
Greek Symbols	
α	heat transfer coefficient between the heated plate and the working fluid flowing in the central mini-channel, $W/(m^2 \cdot K)$
δ	thickness, m
λ	thermal conductivity, $W/(m \cdot K)$
σ_α	mean relative error of the heat transfer coefficient
ΔU	voltage drop, V
Subscripts	
a	ambient air
f	fluid
h	hydraulic
in	at the inlet
IRT	of the heated plate outer surface, measured by infrared thermography
$loss$	heat loss
out	at the outlet
P	plate
w	wall

References

1. Shah, M.M. Chart correlation for saturated boiling heat transfer: Equations and further study. *ASHRAE Trans.* **1982**, *88*, 185–196.
2. Kandlikar, S.G. Fundamental issues related to flow boiling in minichannels and microchannels. *Exp. Therm. Fluid Sci.* **2002**, *26*, 389–407. [CrossRef]
3. Sia, G.D.; Tan, M.K.; Chen, G.M.; Hung, Y.M. Performance enhancement of subcooled flow boiling on graphene nanostructured surfaces with tunable wettability. *Case Stud. Therm. Eng.* **2021**, *27*, 101283. [CrossRef]
4. Bottini, J.L.; Kumar, V.; Hammouti, S.; Ruzic, D.; Brooks, C.S. Influence of wettability due to laser-texturing on critical heat flux in vertical flow boiling. *Int. J. Heat Mass Transf.* **2018**, *127*, 806–817. [CrossRef]
5. Mastrullo, R.; Mauro, A.W.; Viscito, L. Flow boiling of carbon dioxide: Heat transfer for smooth and enhanced geometries and effect of oil. State of the art review. *Int. J. Refrig.* **2019**, *108*, 311–335. [CrossRef]
6. Lin, Y.; Luo, Y.; Wang, E.N.; Li, W.; Minkowycz, W.J. Enhancement of flow boiling heat transfer in microchannel using micro-fin and micro-cavity surfaces. *Int. J. Heat Mass Transf.* **2021**, *179*, 121739. [CrossRef]
7. Goodarzi, M.; Tlili, I.; Moria, H.; Cardoso, E.M.; Alkanhal, T.A.; Anqi, A.E.; Safaei, M.R. Boiling flow of graphene nanoplatelets nano-suspension on a small copper disk. *Powder Technol.* **2021**, *377*, 10–19. [CrossRef]
8. Hong, S.J.; Zheng, X.; Park, C.W. Enhanced flow boiling heat transfer characteristics of R134a on graphene-Cu nanocomposite coating on copper substrate. *Int. Commun. Heat Mass Transf.* **2019**, *108*, 104343. [CrossRef]

9. Cheng, X.; Wu, H. Enhanced flow boiling performance in high-aspect-ratio groove-wall microchannels. *Int. J. Heat Mass Transf.* **2021**, *164*, 120468. [CrossRef]
10. Cheng, X.; Yao, Y.; Wu, H. An experimental investigation of flow boiling characteristics in silicon-based groove-wall microchannels with different structural parameters. *Int. J. Heat Mass Transf.* **2021**, *168*, 120843. [CrossRef]
11. Hsu, W.T.; Lee, D.; Lee, N.; Yun, M.; Cho, H.H. Enhancement of flow boiling heat transfer using heterogeneous wettability patterned surfaces with varying inter-spacing. *Int. J. Heat Mass Transf.* **2021**, *164*, 120596. [CrossRef]
12. Huang, S.; Wang, L.; Pan, Z.; Zhou, Z. Experimental investigation of a new hybrid structured surface for subcooled flow boiling heat transfer enhancement. *Appl. Therm. Eng.* **2021**, *192*, 116929. [CrossRef]
13. Piasecka, M.; Strąk, K.; Maciejewska, B. Heat transfer characteristics during flow along horizontal and vertical minichannels. *Int. J. Multiph. Flow* **2021**, *137*, 103559. [CrossRef]
14. Piasecka, M.; Strąk, K. Influence of the Surface Enhancement on the Flow Boiling Heat Transfer in a Minichannel. *Heat Transf. Eng.* **2019**, *40*, 1162–1175. [CrossRef]
15. Piasecka, M.; Strąk, K.; Grabas, B. Vibration-assisted laser surface texturing and electromachining for the intensification of boiling heat transfer in a minichannel. *Arch. Met. Mater.* **2017**, *62*, 1983–1990. [CrossRef]
16. Maciejewska, B.; Strak, K.; Piasecka, M. The solution of a two-dimensional inverse heat transfer problem using two methods: The Trefftz method and the Beck method. *Int. J. Numer. Methods Heat Fluid Flow* **2018**, *28*, 206–219. [CrossRef]
17. Depczyński, W.; Piasecki, A.; Piasecka, M.; Strąk, K. Impact of Fe powder sintering and soldering in production of porous heating surface on flow boiling heat transfer in minichannels. *E3S Web Conf.* **2017**, *19*, 03012. [CrossRef]
18. Piasecka, M.; Strąk, K.; Maciejewska, B. Calculations of Flow Boiling Heat Transfer in a Minichannel Based on Liquid Crystal and Infrared Thermography Data. *Heat Transf. Eng.* **2017**, *38*, 332–346. [CrossRef]
19. Piasecka, M.; Strąk, K. Characteristics of Refrigerant Boiling Heat Transfer in Rectangular Mini-Channels during Various Flow Orientations. *Energies* **2021**, *14*, 4891. [CrossRef]
20. Kaniowski, R.; Pastuszko, R. Comparison of heat transfer coefficients of open micro-channels and plain micro-fins. *EPJ Web Conf.* **2018**, *180*, 02041. [CrossRef]
21. Kaniowski, R.; Pastuszko, R. Pool boiling of ethanol and FC-72 on open microchannel surfaces. *EPJ Web Conf.* **2018**, *180*, 02042. [CrossRef]
22. Hożejowska, S.; Kaniowski, R.; Pastuszko, R. Application of the Trefftz Method for Pool Boiling Heat Transfer on Open Microchannel Surfaces. *Heat Transf. Eng.* **2022**, *43*, 362–370. [CrossRef]
23. Orman, Ł.J. Enhanced boiling heat transfer on surfaces covered with microstructural mesh coatings. Jordan J. *Mech. Ind. Eng.* **2019**, *13*, 155–160.
24. Available online: https://www.leica-microsystems.com/products/digital-microscopes/p/leica-dcm8/ (accessed on 15 August 2022).
25. Maciejewska, B.; Piasecka, M. Trefftz function-based thermal solution of inverse problem in unsteady- state flow boiling heat transfer in a minichannel. *Int. J. Heat Mass Transf.* **2017**, *107*, 925–933. [CrossRef]